




The Europa Clipper Magnetometer

Margaret G. Kivelson^{1,2}  · Xianzhe Jia² · Karen A. Lee³ · Carol A. Raymond³ · Krishan K. Khurana¹ · Mitchell O. Perley³ · John B. Biersteker⁴ · Jordana Blacksborg³ · Ryan Caron¹ · Corey J. Cochran³ · Olivia R. Dawson³ · Camilla D.K. Harris^{2,3,5} · Jonathan E. Jones³ · Steven Joy¹ · Haje Korth⁶ · Jiang Liu¹ · Elham Maghsoudi³ · Neil Murphy³ · David Parsley³ · David R. Pierce³ · Caroline Racho³ · Ingo Richter⁷ · Christopher T. Russell¹ · Sarah Sherman³ · Robert J. Strangeway¹ · Mickey Villarreal^{3,8} · Benjamin P. Weiss⁴ · Lee Wigglesworth³

Received: 12 October 2022 / Accepted: 18 July 2023 / Published online: 7 September 2023
© The Author(s) 2023

Abstract

Global-scale properties of Europa's putative ocean, including its depth, thickness, and conductivity, can be established from measurements of the magnetic field on multiple close flybys of the moon at different phases of the synodic and orbital periods such as those planned for the Europa Clipper mission. The Europa Clipper Magnetometer (ECM) has been designed and constructed to provide the required high precision, temporally stable measurements over the range of temperatures and other environmental conditions that will be encountered in the solar wind and at Jupiter. Three low-noise, tri-axial fluxgate sensors provided by the University of California, Los Angeles are controlled by an electronics unit developed at NASA's Jet Propulsion Laboratory. Each fluxgate sensor measures the vector magnetic field over a wide dynamic range (± 4000 nT per axis) with a resolution of 8 pT. A rigorous magnetic cleanliness program has been adopted for the spacecraft and its payload. The sensors are mounted far out on an 8.5 m boom to form a configuration that makes it possible to measure the remaining spacecraft field and remove its contribution to data from the outboard sensor. This paper provides details of the magnetometer design, implementation and testing, the ground calibrations and planned calibrations in cruise and in orbit at Jupiter, and the methods to be used to extract Europa's inductive response from the data. Data will be collected at nominal rates of 1 or 16 samples/s and will be processed at UCLA and delivered to the Planetary Data System in a timely manner.

Keywords Europa · magnetometer · Europa Clipper · ocean · induction · calibration · MHD simulation

Acronyms

ACE Advanced Composition Explorer
AFG analog fluxgate magnetometer

Europa Clipper: A Mission to Explore Ocean World Habitability
Edited by Haje Korth, Bonnie J. Buratti and David Senske

Extended author information available on the last page of the article

AIDs	accountability identifiers
CDF	common data format
DFS	Data Flow System
DSN	Deep Space network
ECM	Europa Clipper Magnetometer
EMC	electromagnetic compatibility
EMI	electromagnetic interference
EU	Electronics Unit
FG	fluxgate
FGS	fluxgate sensor
FPGA	field programmable gate array
FRMS	Fault Response Management System
FSC	Flight System Characterization
GDS	Ground Data System
G/RS	Gravity/Radio Science
GNC	guidance, navigation, and control
H&S	health and status
HF	high frequency
IESD	internal electrostatic discharge
IMF	interplanetary magnetic field
iSCLK	instrument clock value
JOI	Jupiter Orbit Insertion
JPL	Jet Propulsion Laboratory
JUICE	JUPiter ICy moon Explorer
Magboom	magnetometer boom
MASPEX	MAss Spectrometer for Planetary Exploration
MHD	magnetohydrodynamic
MLI	multi-layer insulation
MMS	Magnetospheric MultiScale
nT	nano-Tesla
PCDA	power control and distribution assembly
PCB	Printed Circuit Board
PDS	Planetary Data System
PEEK	polyether ether ketone
PI	proportional-integral
PIMS	Plasma Instrument for Magnetic Sounding
PPS	pulse per second
PRM	Pierce-Rowe Magnetometer
PRT	platinum resistance thermometer
PS	power supply
PWA	printed wiring assembly
RDF	radiation design factor
REASON	Radar for Europa Assessment and Sounding: Ocean to Near- surface
RMS	root mean square
RTN	radial, tangential, normal
RWA	reaction wheel assemblies

SADA	solar array drive assembly
SAFA	solar array filter assembly
SDMP	Science Data Management Plan
SIS	Software Interface Specification
SOC	Science Operations Center
sps	sample per second
SRU	stellar reference unit
SUDA	SURface Dust Analyzer
TCM	trajectory correction maneuver
TEC	Total Electron Content
THEMIS	Time History of Events and Macroscale Interactions during Substorms
TID	total ionizing dose
TPSJ	twisted pair shielded jacketed
TUBS	Technical University of Braunschweig
TWTA	traveling-wave tube amplifiers
UART	LVDS Universal Asynchronous Receiver- Transmitter Low-Voltage Differential Signaling
UVS	UltraViolet Spectrograph
VEX	Venus EXpress
VHF	very high frequency

1 Introduction

Europa has a young, icy surface covered with lineaments that appear to be cracks. Gravitational measurements supplemented by modeling indicate that Europa is differentiated, with an iron-rich core and a rocky mantle buried beneath an approximately 100-km-thick layer of water. Although the surface is frozen, it has long been recognized that there may be regions of melt beneath the surface (e.g., Colburn and Reynolds 1985; Kargel and Consovmagno 1996). The hypothesis that part of the icy layer is melted was strongly supported when measurements made by the Galileo mission on a close pass by Europa identified a Europa-centered dipolar field with its pole antiparallel to the concurrent time-varying component of the magnetic field of Jupiter's magnetosphere (Khurana et al. 1998; Kivelson et al. 2000). The magnitude and orientation of the dipole moment were consistent with generation by induction, i.e., by currents driven within Europa by the time-varying magnetic field in its environment. Measurements on a subsequent pass that occurred at the opposite phase of the time-varying field supported the interpretation: the centered dipole had reversed direction (Kivelson et al. 2000; Zimmer et al. 2000). The magnitude of the induced field required currents to flow very near the surface. As solid ice is a poor conductor, the requirement for substantial conductivity led to the conclusion that there must be a global-scale, salty ocean covered by a layer of surface ice.

The compelling evidence for the existence of a buried ocean was based on characterizing Europa's response to time-variations at Jupiter's synodic period (~ 11 hours), which is the only period that could be tested with data from the Galileo encounters. Because the amplitude of a time-varying magnetic field decays inward of the surface of the conductor with a scale-length inversely proportional to the square root of the frequency, there is much to be learned by measuring Europa's response to variations of the ambient field at multiple frequencies. Such measurements can constrain the thickness of the solid ice crust and the conductivity and thickness of the fluid layer. Characterizing these properties to $\pm 50\%$ is one

of the primary science objectives of the Europa Clipper mission (see Europa Clipper Mission overview in this collection), and the Europa Clipper Magnetometer (ECM) is, consequently, a key element of the instrument package.

The naturally occurring frequencies of the field imposed on Europa include Jupiter's synodic frequency and harmonics thereof and the frequency corresponding to the 85.2-hour period of the moon's orbital motion as well as beat frequencies. In order to characterize the responses at multiple frequencies, data will be acquired on tens of encounters over timescales of years, during which the magnetometer measurements will have to be extremely well calibrated and stable. High precision measurement of Europa's induction response, to ≤ 1.5 nT (nanotesla) uncertainty in a field of order 500 nT, is required because the amplitude of the induced field at the critical frequencies varies only slightly as a function of the parameters to be inferred. Both the design and the planned operation of the ECM are focused on achieving the required sensitivity and stability.

The ECM consists of three fluxgate magnetometers spaced along the outer portion of an 8.5-m-long boom provided by Northrop Grumman. The sensors are provided by UCLA and their design and construction rely on heritage from instruments provided for previous successful missions such as Galileo (Kivelson et al. 1992) and Magnetospheric Multiscale (MMS) (Russell et al. 2016). The electronics package, constructed at the Jet Propulsion Laboratory (JPL), is located in the spacecraft avionics vault where it is well protected from the harsh radiation environment near Europa.

Much effort has gone into minimizing magnetic contamination from the spacecraft and the instrument payload. The length of the boom makes it possible to place the outboard sensor reasonably far from spacecraft sources, whose effects fall off as the cube of the separation distance. Small differences in the triad of field measurements made at increasing separation from the body of the spacecraft will be used to determine the effective dipole moment of the spacecraft field, and that unwanted contribution will be removed in order to make it possible for the measurements at the outboard sensor to provide highly precise measurements of the ambient field.

Fluxgate sensors must be calibrated in order to determine the gain, correct for offsets (i.e., the field measured when the external field vanishes), and remove small errors in alignment. The calibration yields a total of twelve parameters for each fluxgate sensor. The magnetometers have been fully calibrated on the ground prior to launch at a special facility operated by the Technical University of Braunschweig, but will require additional calibration during operation, both during interplanetary cruise and after arrival at Jupiter. The calibrations during the orbital phase will require rolling the spacecraft (approximately one hour per rotation) multiple times around two approximately orthogonal axes, typically on every third orbit. Analysis of the data acquired during the rolls will establish 11 of the 12 calibration parameters, but the absolute gain of the sensor triad, although constrained, can only be calibrated on the ground and will not be measured in flight. Fortunately, the primary objective of the magnetometer investigation is to measure the ratio of the magnitude of the inductive response of Europa to the magnitude of the driving field and the absolute gain cancels out in the ratio.

In addition to the measurements that will establish key features of Europa's internal structure, the magnetometer will seek to identify vapor geysers or plumes that are thought to be jetting up intermittently from the surface (Roth et al. 2014; Sparks et al. 2016; Jia et al. 2018). High resolution data will be examined to identify cyclotron emissions from ions picked up as the plasma flows by Europa; such measurements will contribute to the characterization of the neutral atmosphere (Volwerk et al. 2001). Years of data will also give new insight into the dynamics of Jupiter's magnetosphere. The JUICE (JUperiter Icy Moon

Explorer) spacecraft is expected to reach Jupiter while Europa Clipper is in orbit, and this may provide a unique opportunity for two-point measurements either with both spacecraft inside the magnetosphere or with JUICE in the solar wind while Europa Clipper is in the magnetosphere.

In the following sections, critical aspects of instrument design and operation, calibration, data handling and analysis that will extract critical information on Europa's interior are first summarized briefly and then discussed in greater detail. The reader with specialized questions will be interested in the more detailed descriptions; others may wish to skip over those more technical sections.

2 ECM science objectives and requirements

2.1 Ice shell thickness, ocean thickness and conductivity

2.1.1 The induction experiment and associated challenges

The time-varying field at Europa can be represented as a propagating wave. The interaction of an electromagnetic wave with a conductor is governed by the diffusion equation (Parkinson 1983):

$$\nabla^2 \mathbf{B} = \sigma \mu_0 \frac{\partial \mathbf{B}}{\partial t} \quad (1)$$

where \mathbf{B} is the vector magnetic field (external + response) in the vicinity of the conductor, σ is the conductivity of the conductor, and μ_0 is the magnetic permeability of free space. The solutions of this equation for a plane conductor show that the depth to which the wave can penetrate into the conductor, the skin depth, is given by $\delta = \sqrt{2/\omega\sigma\mu_0}$ where ω is the angular frequency of the wave. Lower frequency waves penetrate deeper into a conductor than waves of higher frequency and thus provide information on deeper regions of the conductor. As noted in the introduction and discussed further in Sect. 8.1, Jupiter's rotation and the local time dependence of magnetospheric properties imply that the magnetic field imposed on Europa varies at many predictable frequencies (Khurana et al. 2002; Seufert et al. 2011), and the broad spectrum of fluctuations can be exploited for induction sounding. The longest period magnetic variation relevant to the Europa Clipper mission is excited at the orbital period of Europa (85.2 h) with an amplitude of ~ 20 nT. The strongest signal, at the synodic rotation period of Jupiter (11.2 h), has an amplitude of ~ 250 nT, while its second harmonic (5.55 h) has an amplitude of ~ 20 nT. Europa's interior can be represented as shells of different conductivity surrounding a spherical core. Solutions of equation (1) for time-varying fields imposed on concentric, conducting, spherical shells are well known (Parkinson 1983; Zimmer et al. 2000; Khurana et al. 2009). Because the external field is uniform over the scale size of Europa (order 1 in external spherical harmonics), the response is also of order 1 and, therefore, dipolar.

In Fig. 1a we show the response factor (the secondary field at the surface of the moon at the pole of the induced dipole moment as a percent of the primary field) for several frequencies for a three-layer model of Europa [ice crust ($\sigma = 0$, thickness 20 km), ocean ($\sigma = 2.75$ S) and mantle ($\sigma = 0$)] as discussed in Khurana et al. (2009). It can be seen that both the frequency corresponding to the synodic period and its second harmonic create saturated responses at a level of $\sim 90\%$ for ocean thicknesses larger than 10 km. For large ocean thickness, the amplitude of the induced dipole is near 100% at the top of the ocean.

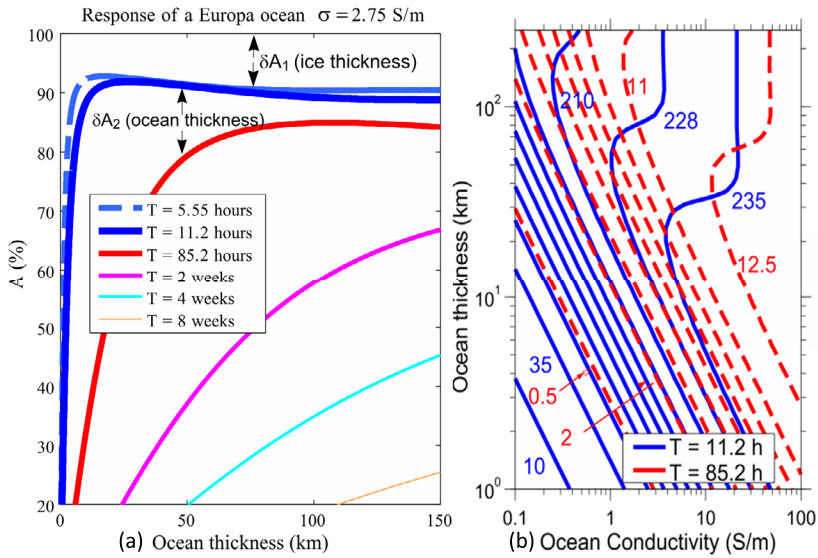


Fig. 1 (a) Response of Europa's ocean as a percentage of the driving field amplitude at the moon's surface at the pole of the induced dipole moment, for a three-shell spherical model, to waves of five different periods for a range of ocean thicknesses. The ocean conductivity is set as 2.75 S/m, which is similar to that of the Earth's ocean. δA_1 ($i = 1, 2$) indicate the primary structural features responsible for reducing the amplitude of the response. (b) The dipolar surface induction field created by the interaction of Europa with Jupiter's varying field at the two principal frequencies ($T = 11.1$ h with amplitude of 250 nT and $T = 85.2$ h with amplitude of 14 nT) for a range of ocean conductivities and shell thicknesses. Both figures adapted from Khurana et al. (2009)

The decrease of dipole field strength with distance reduces the signal from a 100% response and can be used to estimate the ice thickness. In Fig. 1b, reproduced from Khurana et al. (2009), we show the expected induced field (in nT) at the synodic period (blue) and at the orbital period (red) assuming driving field amplitudes of 250 nT and 14 nT, respectively, for a range of ocean thicknesses and conductivities. For ocean thicknesses < 20 km, the contours representing the two frequencies are parallel to each other and cannot be used to determine both the ocean thickness and the ocean conductivity. However, if the ocean thickness is > 40 km and its conductivity exceeds 1 S/m, the two sets of contours intersect, and the intersections can be used to extract unique values of ocean conductivity and thickness with an accuracy better than 50% if the amplitudes of the two harmonics can be determined with a precision of 1.5 nT (the separation of pairs of red dashed lines relevant to the 85.2 hour period in Fig. 1b) or better. Figure 1 also demonstrates that measurements at three or more frequencies can determine all three ocean parameters (depth of burial, thickness, and conductivity).

The induction experiment imposes many challenges to the magnetic field measurements on Europa Clipper. Information on both the inducing field and the dipolar response must be obtained from multiple small segments of data collected when the spacecraft is less than approximately $4 R_E$ ($R_E = 1562$ km is the mean radius of Europa) from Europa's center. For the planned Europa Clipper passes, this condition is met within approximately ± 20 minutes of closest approach. In Sect. 8, we describe an innovative inversion technique that establishes from these intermittent observations the primary (inducing) and secondary (response) fields and thereby infers the relevant properties of Europa's interior. An alternative technique

described in the same section uses Bayesian inference to infer these properties of Europa's ocean by directly modeling the observed signatures.

Magnetic perturbations arise from the interaction between Europa and the flowing plasma of Jupiter's magnetosphere and partially obscure the signal of an internal field. These perturbations can be characterized with considerable fidelity using a magnetohydrodynamic (MHD) model (see Sect. 8.2). The model will be run using measured ambient plasma and field parameters as input to obtain a good approximation to the plasma-generated currents along each flyby trajectory. The associated magnetic perturbations will be subtracted from the measurements, and this will produce a good approximation to the fields that would be found if Europa were located in a non-conducting environment.

An additional significant challenge is posed by the requirement that measurements be highly precise over the roughly three-year primary mission during which the observations are acquired. The zero levels, mutual gains, and the orientations of the sensors must be fully characterized through repeated calibrations. The in-flight calibrations that will provide the required precision are described in Sect. 6. Additional analysis will be performed to establish the contribution of the spacecraft field to the measurements and to remove it.

2.1.2 Complementary measurements

Valuable support for inverting the ECM magnetic field data to establish Europa's interior conductivity profile will be provided by gravity and radar data. In particular, if the depth of the total-H₂O (ice plus water) layer can be constrained by gravity measurements, then the thicknesses of the ice shell and water layer would not be independent parameters in the magnetic inversion process. The H₂O layer thickness can be inferred from the moment of inertia which, in turn, can be determined from the degree-2 sectoral gravity coefficient, C₂₂, if hydrostaticity is assumed. Furthermore, if the degree-2 zonal gravity coefficient, J₂, can be measured with sufficient precision, the hydrostatic assumption can be independently validated (Roberts et al. 2023, this collection). Various analyses of Galileo measurements of the degree-2 sectoral gravity coefficient, C₂₂, give estimates of the thickness of the H₂O shell ranging from ~140 km to 190 km (Schubert et al. 1998, 2004; Jacobson et al. 1999; Casajus et al. 2021). However, because current estimates of J₂ are poor, all of these estimates have required making the as-yet-unverified assumption that Europa is in hydrostatic equilibrium. The Europa Clipper Gravity and Radio Science (G/RS) investigation (Mazarico et al. 2023) is expected not only to provide a more accurate estimate of C₂₂ but also a much more accurate measurement of J₂, thus providing a reliable estimate of the ice shell thickness. Geodesy measurements of Europa's obliquity may yield an independent estimate of the moment of inertia (Roberts et al. this collection).

Other investigations of the Europa Clipper mission, especially the REASON investigation (Blankenship et al. [in prep](#)), will provide additional constraints on the interior structure. The G/RS and Europa Imaging System (EIS) investigations will constrain the degree-2 tidal Love numbers, k₂ and h₂, which in turn depend in part on the ice shell thickness. The Radar for Europa Assessment and Sounding: Ocean to Near-surface (REASON), Europa Ultraviolet Spectrograph (Europa-UVS) (see Europa-UVS paper in this collection), and EIS observations will constrain Europa's shape, and knowledge of the shape will provide an independent constraint on the moment of inertia and elastic thickness, which in turn relate to the ice shell thickness. REASON observations may also identify subsurface layers of liquid or pockets of liquid water in the ice shell. If these are sufficiently thin or discontinuous their inductive response may not be detectable with ECM.

2.2 Relation between conductivity and salinity

Multi-frequency ECM data will impose strong constraints on the conductivity of Europa's ocean. However, the ocean salinity, closely related to its conductivity, is ultimately the parameter of interest for ocean characterization. The salinity can be derived from conductivity only if the salt composition of the ocean is known. Surface composition data combined with geology and geophysical properties will provide information on ocean composition if the ocean chemistry can be disentangled from the confounding overprints of the exchange processes within Europa that bring salts to the surface, exogenically delivered material, and radiolytic processing. Ideally, the dominant salt species in the ocean (likely MgSO_4 or NaCl) will be constrained by surface composition data. In that case, conductivity can be translated into salinity using laboratory data for the range of permissible compositions (e.g., Hand and Chyba 2007; Pan et al. 2021), and via modeling of the lab data to estimate compositions at the temperature and pressure conditions relevant to Europa's ocean (Vance et al. 2021). However, available data for electrical conductivity do not reach the upper bound of models for salt concentration in Europa's ocean, underscoring the need for additional lab data. An alternate, complementary approach would run thermochemical evolution models that start with likely accretionary feedstock to define realistic concentrations of salt species (e.g., Zolotov and Kargel 2009) and ocean and ice shell thicknesses, and would use the outcomes to predict surface and plume compositions. Ranges of possible salinity for both species obtained from these models can be used to define the *a priori* conductivity ranges and thus to bound the parameter space considered using the Bayesian/Markov Chain Monte Carlo inversion of ECM data as described in Sect. 8. While ECM data will provide critical bounds on the conductivity of Europa's ocean, defining ocean salinity inherently requires an interactive modeling effort that must combine geochemical (lab and in-situ) and geophysical data.

2.3 Measurement requirements and planning guidelines

The ECM measurement requirements summarize the detailed properties of the magnetometer data set needed to fulfill key scientific objectives. They specify the cadence of the measurements, their distribution relative to Jupiter's rotation phase and to Europa's orbital phase, as well as the calibration data needed to achieve acceptable levels of uncertainty of the final calibrated measurements. These requirements inform the tour design and are described in the following paragraphs.

Three-axis vector component field measurements are required in order to establish the time-varying field imposed on Europa and to estimate the induced dipole field as well as the plasma-generated fields both remote from Europa and in the proximal regions encountered during flybys. Continuous sampling at 16 vectors/s within a distance of $18 R_E$ relative to Europa is needed to characterize localized plasma-related magnetic perturbations such as possible plume signatures during flybys and to identify pickup ions. (The Jovian field near Europa's orbit is ~ 450 nT, implying an oxygen gyroperiod of ~ 2.3 s and a proton gyroperiod of 0.14 s.) A sampling rate of 1 vector/s provides sufficient temporal resolution to monitor spacecraft fields and instrument stability during intervals outside the flyby periods, and averaging can reduce noise in the ambient field measurements. In order to simplify operations and improve command sequence reusability, we will use ± 2 hours as a proxy for the range ($18 R_E$ from Europa) within which higher time resolution data must be acquired. The range of the magnetic field measurements of ECM is specified as ± 4000 nT, providing for ample margin relative to the range of expected field variations of ± 1000 nT in the vicinity of Europa. For data collected at distances of less than $\sim 18 R_E$ from Europa, the radial

uncertainty of the reconstructed flight system trajectory with respect to Europa's center must be ≤ 1 km. This yields an error in the measured field of less than 1 part in 10^5 so that the uncertainty in the magnitude of a centered dipole of 200 nT will be less than 0.5 nT at 1 R_E and beyond. The orientation of each magnetic field sensor with respect to the IAU-2009 Europa Body Fixed reference frame, including thermo-mechanical distortion and Guidance, Navigation, and Control (GNC) error, is required to change less than 0.385 degrees (6.72 mrad) between consecutive in-flight calibrations. The misalignment will be characterized during the calibration rolls described in Sect. 6.4.

Establishing the induction response with confidence will require measurements within $\sim 18 R_E$ of Europa on multiple passes with closest approach distances of < 110 km. The measurements must sample all phases of the time-varying fields imposed on Europa. There must be at least 12 flybys widely distributed (gaps $\leq 60^\circ$) in System III (1965) (Dessler 1983) longitude in order to determine the amplitude of the induction signal at the 11.2 h period signal. Similarly, there must be at least 12 distributed samples of Europa's orbital phase (true anomaly) with gaps of $\leq 60^\circ$ in order to determine the amplitude of the induction signal at the 85.2 h period. The combination of the induction responses at these two periods is key to determining the ocean thickness and salinity. Continuous data acquisition within ± 15 minutes of closest approach is needed to determine the induction signal at the additional frequencies of interest. In order to develop a high-fidelity model of the magnetic field driving induction at Europa, nearly continuous measurements are required throughout each orbit on which there is an encounter. Data gaps over $\sim 20\%$ of the orbit can be tolerated provided they do not occur within ± 15 minutes of closest approach for each flyby.

To achieve the required ± 1.5 nT measurement uncertainty of the induction response, the individual ECM sensors must be calibrated intermittently in flight in order to detect changes in sensor offsets (zero-levels), gains, and alignments over time (see Sects 6.3 and 6.4). The uncertainty in the measured magnetic field due to the ECM instrument performance is required to be ≤ 1.18 nT after in-flight calibration. Data from spacecraft rolls will provide calibrations that meet the measurement uncertainty requirement. Contributions to measurement uncertainty arise from changes in the sensor calibration, the instrument precision error (digitization noise in the electronics is < 300 pT), and errors in the derived spacecraft field correction. An additional contribution arises from uncertainty in the reconstructed knowledge of the orientation of the spin axis during the roll maneuvers and during the flybys. The frequency of required spacecraft rolls is determined by the anticipated stability of the flux-gate sensors, which has been inferred from the measured drift rate of same-heritage sensors on the MMS mission (Russell et al. 2016). The number of revolutions required to establish the calibration parameters to the desired precision was determined by using model fields augmented by typical noise in Galileo magnetometer data in parts of the magnetosphere just outside of Europa's magnetic shell and analyzing residual errors in the results. A minimum of 6 revolutions about the spacecraft x axis and 6 revolutions about the spacecraft y axis, inbound and outbound to Europa, respectively, was found to be required for full calibration, with no more than 43 days between consecutive x -axis rolls and no more than 43 days between consecutive y -axis rolls. If limitations on the spacecraft power do not allow rolls about two different axes for a given encounter, the x - and y -axis rolls may be executed on consecutive Europa encounters provided that, combined, the separate rolls take place over a Jovian distance range equivalent to that covered in a single encounter with rolls about two axes. The angular error between each of the magnetic field sensor magnetic sensing axes and the spacecraft reference frame is required to be no more than 1.0° . This total angular knowledge error, which includes contributions from spacecraft pointing, boom and sensor alignment stability, will be reduced to 0.1° after analysis of spacecraft roll calibrations.

3 Instrument design: Overview and Description

The ECM comprises three fluxgate sensors, an Electronics Unit (EU), an extendable boom, and a harness connecting the EU located in the body of the spacecraft with the sensors, which are aligned and mounted along the outer portion of the boom. To measure the magnetic field, fluxgate sensors use sets of two highly permeable, ferromagnetic ring cores, which are rapidly driven into oppositely directed saturated magnetization states by a high frequency (8.192 kHz) alternating current applied via toroidal windings on the cores. Each ring core provides measurements in two orthogonal spatial dimensions, and a perpendicular arrangement of two ring cores enables measurements of the three-dimensional magnetic field vector. The time-varying magnetic field generated by each core induces secondary electric currents in a small-scale three-axis Helmholtz coil set surrounding the ring core assembly. In the absence of an ambient magnetic field, the second harmonic of this induction signal is precisely zero. In contrast, an ambient field creates an imbalance in the induction signal, and the second harmonic of this signal is proportional to the projection of the ambient field vector onto the fluxgate sensor axes. The EU is accommodated within the spacecraft avionics vault to protect it from Jupiter's harsh radiation environment and generates the signal to excite the magnetic cores in all three sensors, filters the second harmonic of the voltages induced in the pickup coils, and processes the responses into digital count triplets representing the magnetic field. The digital counts will be converted to physical units of the magnetic field, measured in units of nT, by calibration of the instrument against a reference magnetic field.

The ECM sensors are mounted on an 8.5-m-long extendable boom in order to reduce contributions to the measurements from spacecraft magnetic fields. The use of multiple sensors for the investigation serves two major purposes. First, it allows the characterization of the variable flight system magnetic field as a function of distance from the spacecraft, and it provides for hardware redundancy to provide graceful degradation of the science performance in the event of one, or even two sensor failures. Spacecraft fields at the sensor location decay with distance, r , from the spacecraft as the inverse cube of separation distance, so that the spacecraft field at the end of the boom is reduced by a factor of approximately 1/600 relative to its magnitude at the base of the boom. Differences among measurements made by fully calibrated sensors at different radial distances along the boom (gradiometry) can be attributed to the stray magnetic field from the flight system because the ambient field is spatially uniform across the spacecraft and is thus the same at each sensor. Evidently, the validity of this statement requires that there be no magnetic sources between the sensors.

The choice of sensor positions along the boom must balance the desire to increase sensor separation in order to minimize measurement noise, which increases when sensors are located close together, against the need to place sensors far out along the boom in order to reduce contributions of higher-order (non-dipolar) spacecraft fields, which are significant near the foot of the boom close to the flight system. Sensor positions are also constrained by limitations associated with the boom mechanical design. Optimal sensor positions were determined by minimizing the error in the ambient field recovered from simulated observations using a magnetic model for static and dynamic spacecraft magnetic field sources. As described in Section 4d, the decision to place the sensors at distances 8.5 m, 6.8 m, and 5.2 m from the base of the boom was based on these criteria and a consideration of robustness to the possibility of failure of the outboard sensor. The resulting configuration is illustrated in Fig. 2.

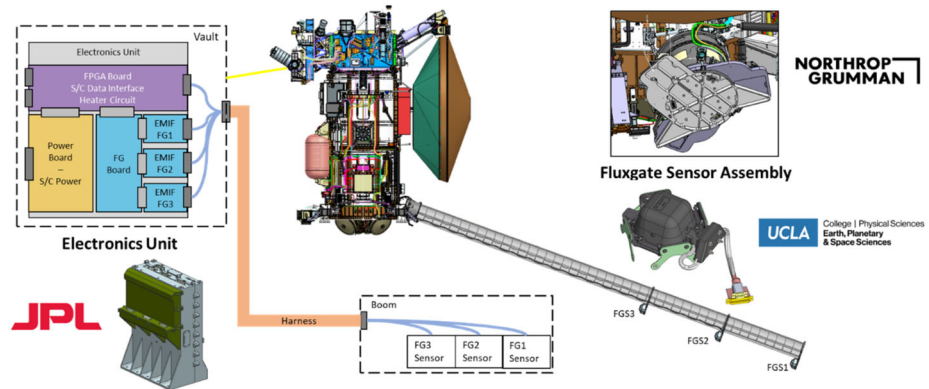


Fig. 2 Europa Clipper Magnetometer instrument overview. The central image shows the spacecraft with the Magboom deployed and the magnetometer sensors located at 8.5 m, 6.8 m, and 5.2 m from the base of the boom. Other images counterclockwise from the top left show a schematic of the Electronics Unit and the harness linking it to the sensor assemblies, the assembled Electronics Unit, a Fluxgate Sensor Assembly and its harness, and the magnetometer boom in its stowed configuration

3.1 Instrument system engineering overview

The instrument and deployable boom designs focused on implementation of existing capabilities of space magnetometers, as demonstrated past performance proved sufficient for accomplishing the desired measurements at Europa. Nonetheless, existing designs required tailoring to ensure compatibility with the Europa Clipper spacecraft and the space environments to be encountered during the mission. Electromagnetic interference and internal electrostatic discharge compatibility, magnetic cleanliness, thermo-mechanical and thermal stability of the fluxgate sensors (FGS) and the boom, and protection from the extreme radiation environment present near Europa required special attention.

The manufacture of four major components of the ECM was a coordinated effort:

- three tri-axial fluxgate magnetometer sensor assemblies were designed and manufactured as a collaboration between UCLA and JPL;
- low noise electronics were designed and manufactured by JPL using a heritage UCLA design;
- cables were designed and manufactured at JPL; and
- the deployable boom was designed and manufactured by Northrop Grumman.

As noted, ECM utilizes technologies with extensive flight heritage for each subsystem. The FGS head, designed and fabricated at UCLA, has decades of space flight history. The FGS uses no active electronic components and features custom shields to protect the sensor assembly from both radiation and electromagnetic interference (EMI). Integrated non-magnetic heaters and multi-layer insulation (MLI) maintain the sensors' temperatures for stable performance, and the power of the operational heater is modulated at high frequency to avoid interference with magnetometer drive, feedback, and sense signals. The FGS details are discussed in Sect. 5.1.

The Electronics Unit (EU) implements a Pierce-Rowe magnetometer architecture (Russell et al. 2016) within a complement of six printed wiring assemblies (PWAs): three EMI filter PWAs, one for each FGS, the fluxgate (FG) PWA for processing the analog signals to and from the three sensors, the field programmable gate array (FPGA) PWA to perform

analog-to-digital conversion and digital processing, and the power supply (PS) PWA that conditions the power distributed from the spacecraft bus. The details of the EU are discussed in Sect. 5.2.

Spanning approximately 15 m in length, multiple twisted pair shielded jacketed (TPSJ) lines in 10 different cables connect each of the three sensors to the electronics unit. Particular care was taken with shielding, wire gauge, flexibility, and other factors described in Sect. 5.4.

The magnetometer boom (also referred to as Magboom or boom), supplied by Northrop Grumman, is an 8.5 m coilable boom akin to magnetometer booms that have previously flown in space. The structure holds two mid-rings where the middle (FGS-2) and inboard (FGS-3) fluxgate sensors are supported, and one tip-plate that supports the outboard fluxgate sensor (FGS-1). The boom structure is stowed inside of a canister that hosts the mechanisms and thermal control hardware to execute deployment. The details of the boom design are discussed in Sect. 5.3.

The Europa Clipper spacecraft mechanically accommodates ECM hardware in two distinct physical locations and along paths where intra-instrument cabling is routed. The lower propulsion module supports the magnetometer boom canister mounted on struts; the protective radiation vault hosts the electronics unit; and the ~ 15 m instrument cable harness extends from the vault to the coilable boom and sensors, across the spacecraft's Avionics and Propulsion Modules. The spacecraft electrically accommodates ECM by providing redundant power and serial data interfaces. The EU receives commands and transmits science and engineering telemetry data packets to the avionics subsystem.

The ECM is designed to operate continuously, with simple commands to power on and specify a limited number of parameters for data collection, and an autonomous capability to request the avionics to power-off or reset the instrument in response to fault indications. When the magnetometer is not operating, the spacecraft monitors the fluxgate sensor temperatures and energizes appropriate heaters if a sensor temperature falls below the allowable range. The services needed for the one-time deployment of the boom are also provided by the spacecraft, including power to heaters that will warm the canister to the deployable temperature range, power to the heater for release of the frangibolt restraint mechanism, and telemetry needed to assure safe and successful deployment. Internal instrument and external spacecraft interfaces are shown in the ECM instrument block diagram (Fig. 3). Relevant instrument characteristics are summarized in Table 1.

3.2 Instrument performance

3.2.1 Error budget overview

The investigation's science error budget shown in Table 2 is derived from the Level-2 science requirement that the measurements must be sufficiently precise to assure a residual uncertainty of no more than ± 1.5 nT for the magnetic induction response determined from data reduction from all flybys. The requirement is broken into two parts: Calibrated vector data uncertainty and reconstructed sensor attitude knowledge error. Each part is computed from the root of the sum of the squares of the contributions, and the parts are added to provide the overall error.

The calibrated vector data uncertainty refers to the portion of the error budget contributed by the magnetometer system performance. It includes parameters affecting the sensor stability (offset, gain, and alignment), electronics noise, spacecraft field correction, and the in-flight calibration uncertainty, which is the major contributing factor. The instrument design and tests are driven by the objective of ensuring the delivery of a stable magnetometer

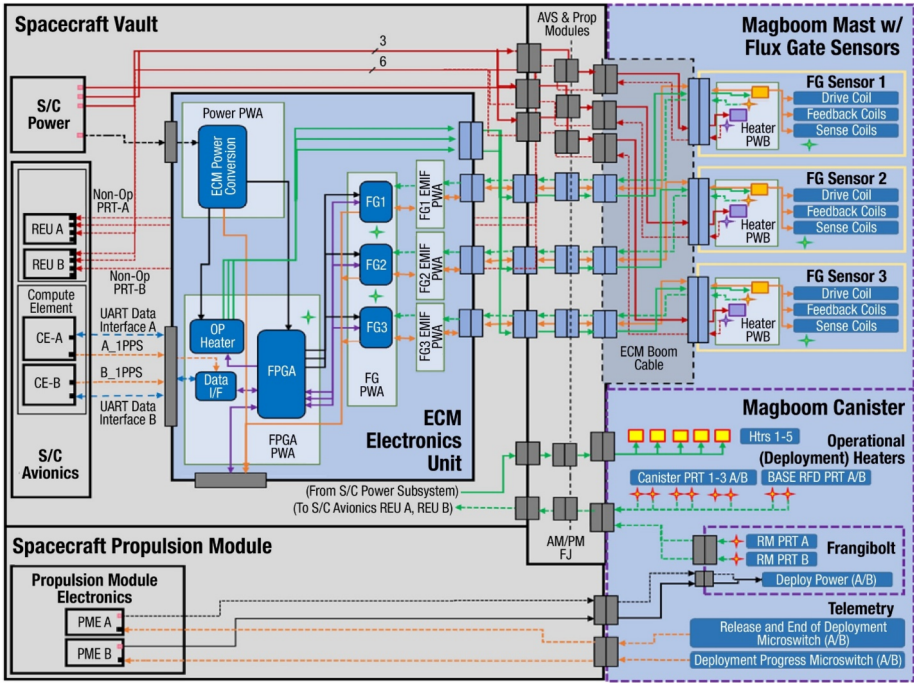


Fig. 3 ECM functional block diagram. Blue panels represent the ECM instrument components. ECM electronics interface with Europa Clipper Power and Avionics subsystems inside the Spacecraft Vault. FG sensors electrically interface with the ECM electronics and the Magboom deployment is controlled by the spacecraft. Fluxgate sensors are controlled by the ECM electronics, except for non-operational heaters and thermometers within the sensor assemblies

system. Ground calibrations, in-flight calibrations, and science data post-processing will reduce the uncertainty in the data to be used for scientific analysis.

The two principal contributions to the error budget for the vector magnetic field measurements are the instrument’s precision and the attitude knowledge of the sensors. The instrument precision is determined by the stability of the system, the accuracy of the calibration, and the instrumental noise. The fluxgate sensors’ gains, offsets, and alignment and their variation with temperature have been calibrated against an absolute reference on the ground prior to integration with the spacecraft. Additional calibrations will occur during cruise when predictable properties of the solar wind will be used to provide a useful assessment of the offset changes over time. Relative sensor calibrations will be established repeatedly during the tour using observations taken during flight system rolls about two orthogonal spacecraft axes, scheduled on average approximately every 42 days. The calibration parameters vary with thermo-mechanical distortions of the sensor structure that may occur between in-flight calibrations. The instrumental noise is largely determined by the material properties of the sensors’ magnetic cores. Uncertainties in the reconstructed knowledge of the sensor attitude are the primary sources of error. These uncertainties include the small inaccuracy in the flight system attitude determined by the stellar reference units (SRUs), misalignment between the sensors’ mechanical and magnetic axes, and any thermo-mechanical distortions aggregated between the SRUs and the fluxgate sensors. The former two contributions are fixed and can be inferred from and corrected using spacecraft rolls, but instabilities of the

Table 1 Europa Clipper Magnetometer resources and nominal performance characteristics

Dimensions	Sensor	20.6 cm × 20.9 cm × 11 cm
	Electronics	27.1 cm × 21.0 cm × 13.6 cm
	Boom (stowed)	38.8 cm length × 87.0 cm diameter
	Boom (deployed)	8.5 m length × 87.0 cm diameter
Mass	Each sensor	1.3 kg
	Electronics	4.5 kg
	Boom	25.0 kg
	Intra-Instrument Cable	11.5 kg
	Total	45.0 kg
Power	Instrument with FGS Operational Heaters	18.0 W
	FGS Operational Heater	1.1 W typical
	FGS Non-Operational Heater	1.2 W
	Magboom Deployment Heaters	111 W for 8 hours at 27.8 V
Noise	Low Noise Tri-Axial Fluxgate	<20 pT/ $\sqrt{\text{Hz}}$ at 1 Hz intrinsic noise level
Stability	FGS Temperature	± 0.25 C
	Offset (average value)	0.10 nT based on MMS data
	Scale Factor (average value)	0.20 nT based on MMS data
Analog-to-digital converter	20-bit Sigma Delta with 4096 conversions per second	
	Nine (9) independent units, one for each axis on each magnetometer	
Range	Of order ± 4000 nT full scale	≈ 8 pT resolution (20 bits output)
Output Data Rates	Low Rate	1 Hz
	Normal High Rate	16 Hz
	Highest Rate	128 Hz

boom, although expected to be small, may not be correctable. Inaccuracy in estimation of the spacecraft magnetic field also contributes to the measurement error.

The ECM science error budget of Table 2 assumes a 500 nT background field, roughly that present near Europa's orbit. The aforementioned sources of error are split into "Calibrated Vector Data Uncertainty" and "Reconstructed Sensor Attitude Knowledge Error." The error for each category and the total error are computed as the root-sum-square of the tabulated values, and the overall uncertainty of the individual magnetic field measurements amounts to 1.83 nT. It has been shown by analysis (cf. Sect. 8) that despite this small uncertainty, it will be possible to determine Europa's induction response to within ± 1.5 nT from measurements acquired over multiple flybys (see Sect. 2.1.1) and thus to meet the Level-2 science requirement of the Europa Clipper mission.

3.2.2 Magnetometer performance (range, resolution, stability, noise)

The induction science for the ECM must resolve the relatively small induction response with considerable precision at a number of different frequencies. Fortunately, the design of the fluxgate magnetometers, based on magnetometers flown at the Earth as part of the MMS mission (Russell et al. 2016) and also required to meet stringent scientific requirements,

Table 2 ECM Science Error Budget

Magnetic Field Uncertainty Contribution	Error [nT]	Error [mrad]
Vector Data Uncertainty (random) – RSS of errors below	1.18	
Sensor offset stability	0.10	
Sensor gain stability	0.20	
Sensor alignment stability	0.10	
Precision error (derived from sensor noise)	0.30	
In-flight calibration uncertainty (derived-post calibration rolls)	1.00	
Spacecraft field correction (derived)	0.50	
Reconstructed sensor attitude knowledge error (partially systematic) - RSS of errors below	1.39	2.83
Stellar Reference Unit to boom mechanical stability	0.27	0.54
Boom to sensor mechanical stability	1.11	2.22
Sensor mechanical to sense axis	0.66	1.33
GNC knowledge	0.43	0.87
Total magnetic field error (RSS Vector Data Uncertainty and Reconstructed Sensor Knowledge Error)	1.83	

was available as a point of departure. The MMS magnetometers were able to resolve the ambient magnetic field with high precision in regions where the magnetic field essentially vanishes as its energy and momentum is transferred to the ambient plasma. Furthermore, the magnetometers were able to establish differences among the fields measured in Earth's magnetosphere at four spacecraft separated by distances as small as 10 km, which is an exceptionally challenging objective. The MMS magnetometers had two dynamic ranges: ± 8000 nT (high range) and ± 500 nT (low range), a noise level of ~ 10 pT/ $\sqrt{\text{Hz}}$ at 1 Hz in low range, and an accuracy of 100 pT (primarily determined by offsets). Given the similarity of field ranges to those that will be encountered by Europa Clipper and similar sensitivity requirements, the MMS sensor design provided an ideal basis for the design of the ECM sensors. The MMS electronics design was modified to use a sigma-delta implementation of the high-resolution analog to digital conversion, referred to as the Pierce-Rowe Magnetometer (PRM). This design has also been implemented in the magnetometer for the InSight mission (Banfield et al. 2019), which acquired data on the surface of Mars. The sigma-delta modulation in the PRM provides high resolution and high integration analog-to-digital conversion of the signals with low power consumption.

The MMS and InSight heritage gives high confidence that ECM can meet the measurement requirements of ± 4000 nT dynamic range, 50 pT/ $\sqrt{\text{Hz}}$ at 1 Hz noise, and alignment knowledge to within 0.25 degrees (4.36 mrad). The materials' selection and the mechanical design of the sensor assembly and mounting interface tightly restrict angular rotations arising from differential coefficients of thermal expansion. Noise levels are partially set by matching electronics and sensor, but the intrinsic properties of the sensor core material also determine the noise level. The sensor cores were carefully selected from a large number of available cores to provide the best possible instrument properties. Prior to delivery to JPL, the three flight sensors showed noise levels of approximately 15 pT/ $\sqrt{\text{Hz}}$ at 1 Hz, implying an integrated precision error of 300 pT. These sensors had not yet been matched with their flight electronics boards. Prior to system integration, gains, offsets, and internal alignment (sense axes to mechanical axes) were determined at the Technical University of

Braunschweig (TUBS) calibration facility as discussed in Sect. 6.1. Although offsets and alignments will again be determined during the cruise phase of the mission, and on orbit at Jupiter, a strict magnetic cleanliness program has been implemented to ensure that the sensors are not exposed to magnetizing fields before or after the TUBS calibration activity.

3.2.3 Thermo-mechanical stability

As noted above, a critical requirement for achieving the goals of the ECM investigation is to assure the thermo-mechanical stability of the magnetometer system. Early in the ECM program, the mechanical and system engineering teams worked in tandem with the science team to develop a complete error budget, an effort that required identifying the thermo-mechanical distortions that affect the investigation. Because the in-flight alignment changes will be characterized during the calibration rolls, validation and verification activities to be performed on ground are drastically simplified; classical analytical methods that neglect gravity distortion suffice to validate the alignment error. The stability errors that remain after calibration rolls are fourfold: 1) sensor mechanical to sense axis (the largest contribution), 2) boom to sensor mechanical axis, 3) SRU to boom mechanical axis, and 4) GNC knowledge.

The science and reconstructed knowledge error budgets have been continually updated throughout the design and development phase of the program as analysis and test data have been refined. This effort included thermal distortion analysis of a high-fidelity finite element model subjected to the predicted thermal environment during science data collection near Europa. These detailed model refinements have reduced the uncertainty to the levels summarized in Table 2.

4 Instrument design: Special challenges and considerations

Special challenges to instrument performance arise because of the thermal and radiation conditions of the natural space environment in which ECM must survive and perform and because of both DC and AC signals arising from the spacecraft and its suite of instrumentation. The harsh radiation dose, space charging, and cryogenic and transient thermal environments at Jupiter drive many aspects of the ECM design, including materials selection, grounding configuration, and protective covers. In addition, the spacecraft subsystems and payloads, in particular a radar instrument operating with high transmit power and highly sensitive receivers, require substantial filtering to ensure electromagnetic compatibility.

4.1 Radiation and IESD

High-energy electrons and protons trapped in Jupiter's magnetic field create a radiation environment that is particularly intense near Europa's orbit. Magnetometer components have been selected to operate within specification during and after the exposure to the anticipated total ionizing radiation dose with a radiation design factor (RDF) of twice the level expected at the location of the device. The boom, surrounded by its thermal sock, is designed to withstand a total ionizing dose (TID) 220 Mrad(Si). The fluxgate sensor assemblies have been designed to withstand over 44 Mrad(Si), which is the dose predicted beneath the thermal blankets (Andersen et al. 2020). The Europa Clipper spacecraft employs a radiation shielding vault to house electronics that cannot survive the harsh environment; the ECM EU is situated within this spacecraft avionics vault and is designed to be robust to a TID exposure of up to 300 krad(Si).

Plasma environments encountered during the Europa Clipper mission may lead to surface charging and create the potential for internal electrostatic discharge (IESD), which occurs when highly energetic electrons penetrate dielectric material and discharge from some depth within, causing uncontrolled arcing and structural failure of the material. Mitigations for such failures impose additional design constraints. Floating conductors and dielectrics used in the ECM have been assessed for internal charging where it was not possible to provide a static bleed path to spacecraft ground. The magnetometer development team carried out an extensive test and analysis program to characterize discharge pulses that arise from the sensors under bombardment with energetic electrons and to analyze their propagation along the cables to assess the voltage and energy at the electronic components inside the vault. Electronic parts at the vault interface have specifically been selected with voltage and current ratings that withstand the predicted pulses.

4.2 EMI effects and grounding (EU, FGS, Magboom, cables)

Electromagnetic compatibility (EMC) among elements of the Europa Clipper flight system is critical to the successful achievement of mission's science objectives. The most challenging compatibility requirements arise from interactions between ECM and REASON. ECM's Magboom-mounted sensors and cables fall in the field of view of the REASON antennas, creating unavoidable interaction with REASON's chirped high frequency (HF) and very high frequency (VHF) pulses. Radio frequency modeling shows that during REASON HF transmissions, the fields imposed at ECM's outboard sensor are particularly intense at 9 MHz, the frequency at which the 8.5 m Magboom assembly approximates a quarter-wavelength resonator (see Fig. 4). The most difficult electromagnetic compatibility design challenge for ECM has been to maintain signal precision and integrity in the presence of REASON transmissions, with susceptibility to a radiated electric field at the outboard sensor in the 8.5 to 9.5 MHz range set to 65 V/m, which includes a standard 6 dB EMI/EMC modeling margin. Conversely, REASON's ultra-sensitive receivers demand that radiated emissions from ECM remain below -4 dBuV/m in the 8.5 to 9.5 MHz HF notch, and below -8 dBuV/m in the 55 to 65 MHz VHF notch.

The stringent emissions and susceptibility requirements prompted risk reduction testing with early prototypes of the magnetometer system to evaluate the effectiveness of cable and sensor shielding and to understand the magnitude of the residual interference to be attenuated by EMI filters. This testing showed that predicted levels and modulation from REASON transmitters produced offset changes in magnetometer science data. Susceptibility occurred only when radiated fields were modulated at specific frequency bands in the range of the radar's pulse repetition rate. A carbon fiber EMI shield cover placed over the sensor reduced the direct coupling into the FGS coils and wiring by 20 dB. The radiated emission from the prototype cabling and sensor were also measured in order to quantify the attenuation required from the EMI filters so that emissions radiated from the Magboom and Propulsion Module cables and the sensors remain below REASON's susceptibility limits. Because electromagnetic modeling at long wavelengths is difficult to validate and because tests were conducted on prototype subsystems with cabling that may differ from the flight instrument, a large number of uncertainty terms were used in constructing the model and allocating the EMI attenuation budget.

The prototype testing confirmed the need to incorporate a specially designed EMI enclosure to shield each FGS (cf. Sect. 5.1) and to insert EMI filters in the EU for further rejection of unwanted signals (cf. Sect. 5.2). In addition to shielding and filtering, grounding measures were implemented to drain ultrahigh radio frequency currents and isolate relatively large drive signals from the sensitive sense and feedback lines.

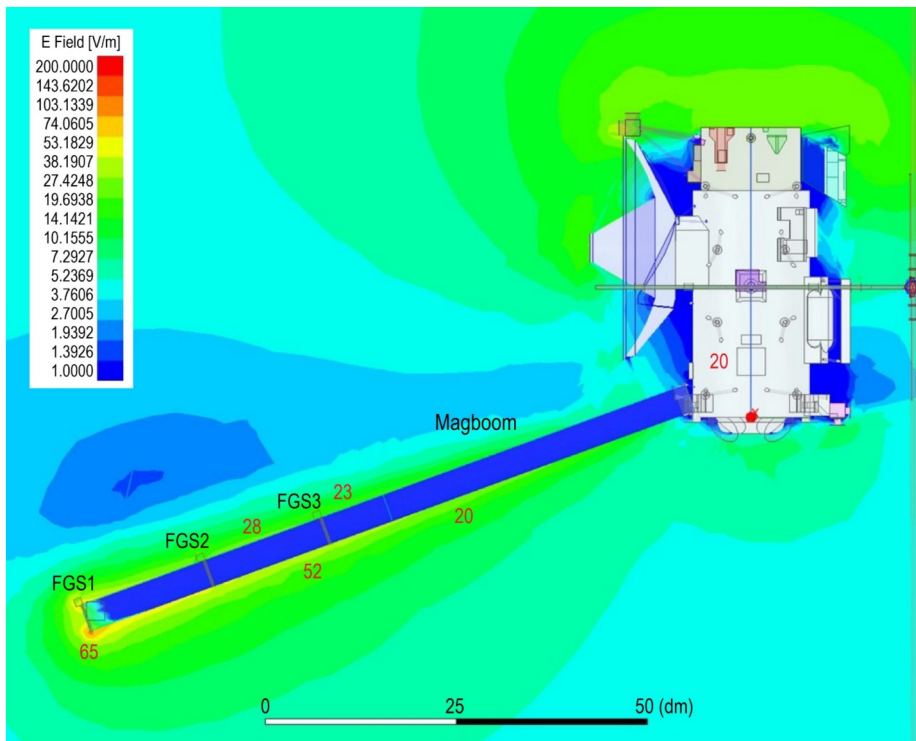


Fig. 4 HF (9 MHz) field intensity predictions for ECM. Electric fields during times when the REASON radar instrument is transmitting are predicted to be as high as 65 V/m in the vicinity of ECM's outboard sensor. Grounded shields to attenuate the incident field and EMI filters to reject the remaining unwanted signal have been designed to mitigate this interference

4.3 Spacecraft magnetic cleanliness

Multiple magnetic field sources on the highly complex Europa Clipper spacecraft can potentially interfere with the magnetic induction investigation of Europa's subsurface ocean. The mission team includes a dedicated EMI and EMC group responsible for ensuring that spacecraft fields are kept to a minimum by verifying that all components, subsystems, and instruments are designed and built with good magnetic cleanliness practices, including the use of non-magnetic materials, use of twisted-pair wiring, and solar array back-wiring to reduce the induced magnetic field associated with large current sources. The EMI/EMC team attempts to minimize the stray magnetic fields originating from the large field sources that are unavoidable in the design of the spacecraft by using compensation magnets or highly permeable shielding (e.g., mu-metal).

The most significant dynamic magnetic field sources on the spacecraft are the power system batteries, the AC currents on the rotating solar array, the power control and distribution assembly (PCDA), the solar array filter assembly (SAFA), and the solar array drive assembly (SADA). The four reaction wheel assemblies (RWA) located near the base of the magnetometer boom create a lower amplitude dynamic signal but cause concern because of their variable frequency.

Table 3 Constraints on spacecraft sources of DC and AC magnetic fields at the outboard FGS located at the end of the magnetometer boom (~8.5 m from the edge of spacecraft)

Frequency Range	Peak to peak amplitude	Notes
DC (0 Hz)	1 nT	Contribution from remanent magnetization
0.0001 Hz < $f \leq$ 0.05 Hz	283 pT	Typical rate of solar panel rotations and illumination changes
0.05 Hz < $f \leq$ 5 Hz	100 pT	Typical spacecraft-generated AC field
5 Hz < $f \leq$ 5 kHz	50 pT	
5 kHz < $f \leq$ 20 kHz	503 pT	This band includes the sensor drive and second harmonic frequencies
20 kHz < $f \leq$ 100 kHz	5030 pT	The magnetometer response to field fluctuations above 20 kHz is not significant.

Other dynamic magnetic sources that could contribute undesired signals include the RF switches and the traveling-wave tube amplifiers (TWTA) associated with the telecom system. In order to meet the ECM Level-2 science objective, both the AC and DC magnetic field spacecraft signatures affecting the investigation must be kept as small as possible. The requirements for the outboard sensor, translated into peak magnitudes within different frequency bands, are listed in Table 3. The AC requirements are provided in different frequency bands because different frequency ranges are measured and verified in different ways.

As it is nearly impossible to verify these magnetic requirements for the entire spacecraft system in the flight configuration on the ground (because of difficulties in nulling out Earth's field and stray magnetic fields and the need for deployed solar array and boom, etc.), maximum magnetic moment allocations are assigned to all potential DC and AC currents and material sources (subsystems, instruments, and magnetic mechanical structures) on the spacecraft. Each source is independently measured by the EMI/EMC team using multiple magnetometers positioned around the component so that an effective dipole magnetic moment can be extracted from the measurements. This information is gathered in a spreadsheet in which each magnetic source is represented by a magnetic moment magnitude, orientation, and position on the spacecraft. The resulting model is used to estimate the aggregate magnetic field at any position around the spacecraft, and, in particular, at the locations of the FG sensors and the Faraday cups of the Plasma Instrument for Magnetic Sounding (PIMS) (Westlake et al. 2023 this collection). The suitability of this multiple dipole approach has been validated for previous missions (Neubauer and Schatten 1974; Mehlem 1978a,b; Zhang et al. 2007; Mehlem and Wiegand 2010).

The magnetic field model of the spacecraft includes more than 400 dipole sources. The magnetic moments were measured or estimated based on heritage data, subject matter expert assessment, or vendor product information. Early in the development phase, the orientation of the estimated magnetic moments was not known, implying that the magnetic field imposed by individual dipole moments on the sensors was uncertain both in orientation and to within a factor of two in magnitude. Therefore, the total magnetic field contributed by all sources on the spacecraft (see Fig. 5) at the location of the outboard sensor was modeled using a Monte Carlo simulation. In the simulation, the magnitude and location of each magnetic moment identified on the spacecraft was fixed but its orientation was allowed to vary. The orientations of all magnetic sources were randomized 10^5 times to provide sufficient variation of moment orientations to produce a meaningful estimate of the range of possible superpositions of the magnetic field sources. In the simulation, the dipole magnetic field B_j

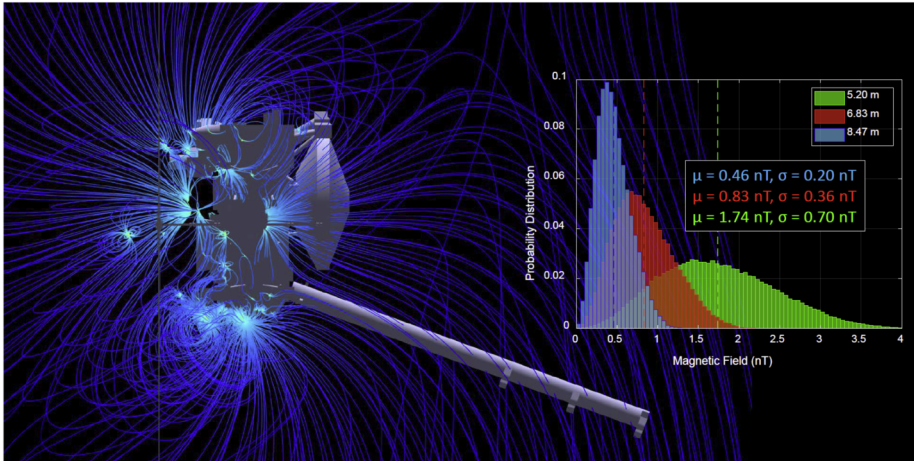


Fig. 5 Schematic of field lines arising from identified magnetic sources on the spacecraft. Insert: Probability distributions of the magnitude of the spacecraft field at three sensors at locations 5.2 m (green), 6.8 m (red), and 8.5 m (blue) along the boom

at sensor j is given by,

$$B_{sc,j} = \frac{\mu_0}{4\pi} \sum_{i=1}^N \frac{3 [(\mathbf{r}_j - \mathbf{r}_{M_i}) \cdot \mathbf{M}_i] (\mathbf{r}_j - \mathbf{r}_{M_i}) - \mathbf{M}_i |\mathbf{r}_j - \mathbf{r}_{M_i}|^2}{|\mathbf{r}_j - \mathbf{r}_{M_i}|^5} \quad (2)$$

where \mathbf{r}_j is the position of sensor j in spacecraft coordinates, and \mathbf{M}_i is the magnetic moment of the i th spacecraft magnetic component centered at position \mathbf{r}_{M_i} . The insert in Fig. 5 illustrates the distribution of the magnitudes of the simulated magnetic field at ECM sensor positions, 5.2 m, 6.8 m, and 8.5 m along the boom. The average field at the outboard sensor is 0.46 nT but can be as high as 1.05 nT (3-sigma). This range of values is compatible with the requirement that measurement precision be better than 1 nT because the dominant contribution of the spacecraft field will be removed from the data by in-flight characterization of its dipole moment using differences in the measured values at sensors spaced along the boom.

The AC magnetic field limits have not been simulated because of the large range of frequency and phase characteristics possible for each field source. In order to ensure that the AC requirement is met at the outboard sensor, each individual AC magnetic field source will be tested to confirm that it meets the allocation specified in the spacecraft magnetic field model kept by the EMI/EMC team. If individual AC magnetic field sources do not exceed their individual magnetic moment allocations, their sum total will remain below the required limit specified in the ERD, even if all field sources add constructively (i.e., contribute noise at the same frequency and phase).

4.4 Selected sensor locations on the magnetometer boom

To our knowledge, the ECM investigation will be the first spacecraft magnetometer investigation to characterize the spacecraft field using gradiometry with more than two sensors. The primary sensor is ideally placed on the end of the boom, but a key design choice that

affects the performance of the ECM gradiometer is the positions of the two inboard sensors along the boom. Because of the structure of the boom, sensors can be mounted only to static end terminals at the end of each bay. The bays of the coilable boom are spaced 0.185 m apart and provide a total of 46 discrete possible positions for sensor placement. In order to reduce crosstalk of neighboring sensors, a minimum spacing of 0.7 m is required. Finally, the three sensors must be placed so that they do not physically interfere with one another when the boom is in its stowed or deploying configurations, which further limits the number of acceptable combinations of sensor locations. One configuration that is ideal from a mechanical perspective places the sensors at positions previously noted (Sect. 4.3). What makes this sensor configuration particularly attractive is that it not only satisfies the mechanical constraints, but it also provides acceptable (though not truly optimal) sensor separations for gradiometry and places the middle sensor near the outboard sensor, providing redundancy in case of an outboard sensor failure.

4.5 Sensor thermal control and stability

In order to achieve the required measurement precision, the temperature at the magnetometer sensor core is required to be stable within a range of ± 1 °C. The FGS thermal interaction with the environment depends on the power dissipated in the sensor coils, the conductive heat transfer to the sensor from the heaters, heat losses through mechanical interfaces to the Magboom and cabling, and radiative heat transfer views that vary with spacecraft orientation during the mission. The largest rate of change of temperature that must be controlled by the thermal system will occur before and after each close approach to Europa. In this critical portion of each orbit, the FGS to Magboom interface temperature is predicted to change as much as 20 °C over a period of approximately 8 hours. A thermal balance test using prototype electronics and an engineering model FGS demonstrated the thermal control system's ability to maintain the sensor core temperature within ± 1 °C of the set point. Additional aspects of thermal design are described in Sects. 5.1 and 5.5.

5 Instrument components: description and implementation

5.1 Fluxgate sensors (FGS)

5.1.1 Design overview

The UCLA-heritage FGSs must operate at ambient temperatures (+60 °C in the inner Solar System to -120 °C in Jupiter orbit) that are both lower and higher than those encountered by the sensors on the MMS and Insight missions, on which their design is based. They must also survive and maintain performance in the challenging environment of Jupiter's magnetosphere discussed above. These challenges required modification of the design of precursor instruments.

The ECM sensor head (Fig. 6), based on UCLA-heritage designs, is assembled using structural elements fabricated from a custom PEEK (polyether ether ketone) plastic loaded with carbon nano-tube particles in order to survive the radiation environment and to dissipate charge for IESD mitigation. Each sensor head consists of several parts, as shown in Fig. 6. The interior assembly consists of the drive and sense coils. Armatures house the interior assembly and support the PWAs that act as an interface between the magnet wire windings in the sensor and the "pigtail" harness that exchanges signals with the EU in the

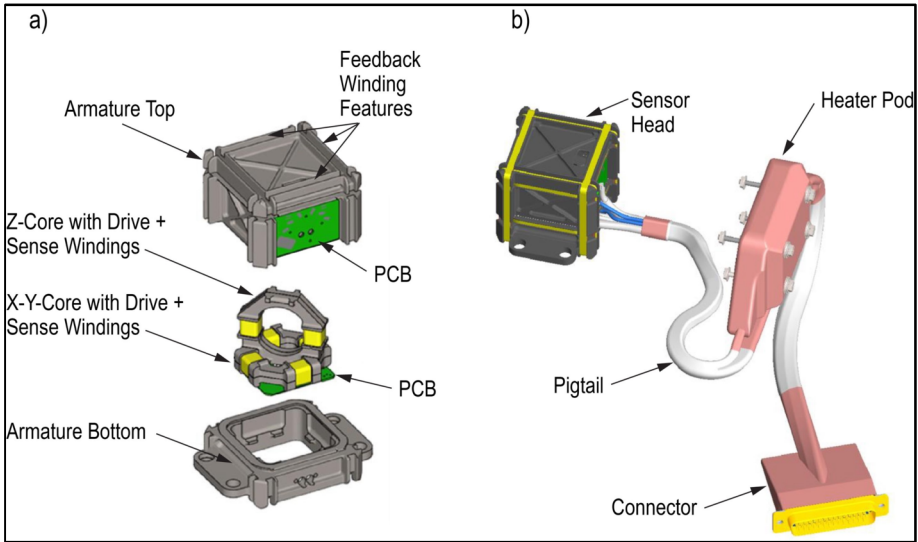


Fig. 6 Fluxgate Sensor Assembly. **(a)** Exploded view shows the constituent parts of the fluxgate sensor head; **(b)** the assembled sensor head is integrated with its pigtail harness and heater pod before mounting to the base plate and installing EMI and radiation shields

vault and, in the ECM design, thermally couples the sensor to the heater PWA. The armature assembly also includes feedback windings that null the exterior magnetic field. This implies that the sensor itself operates in a near zero field, providing a highly linear response, with the feedback signal providing a measurement of the external field. This implementation of a fluxgate magnetometer is often referred to as a closed loop design.

In order for the fluxgate cores to perform with sufficiently low noise to meet requirements and to survive in the event of the spacecraft entering safe mode, the ECM sensor head assembly must remain at a temperature above -120 °C. Magnetometers on space missions have used non-magnetic, radioactive sources to produce heat for spacecraft systems but Europa Clipper mission guidelines prohibit use of radioactive materials. For this reason, the ECM sensor heater design relies on resistive heating using non-magnetic thick-film resistors qualified for the Jovian environment and screened for flight. The resistor networks that separately provide heat for both operational and non-operational conditions are mounted to a single PCB (Printed Circuit Board) located a few inches away from the sensor head. The assembly comprising this PWA and its shielding enclosure is the heater “pod” (see Fig. 6b and 7). Heat dissipated on the heater PWA by the resistors is conducted via copper wire in the pigtail to the sensor head in the immediate vicinity of the cores. Platinum resistance thermometers (PRTs) on the heater PWA provide temperature knowledge to the ECM EU and to the spacecraft avionics for control of the sensor survival heater. A single PRT in the sensor head (mounted to one of the PCBs) provides temperature feedback for FGS thermal control.

In order to protect the system from low frequency electromagnetic signals, the FGS pigtail harness is shielded with a braided overshield and copper tape. Black Kapton tape over-wrap provides additional protection from IESD events potentially generated by dielectrics in the harness (see Sect. 4.1). The heater pod is also wrapped in copper tape to serve as an EMI shield with the pigtail and a ground path.

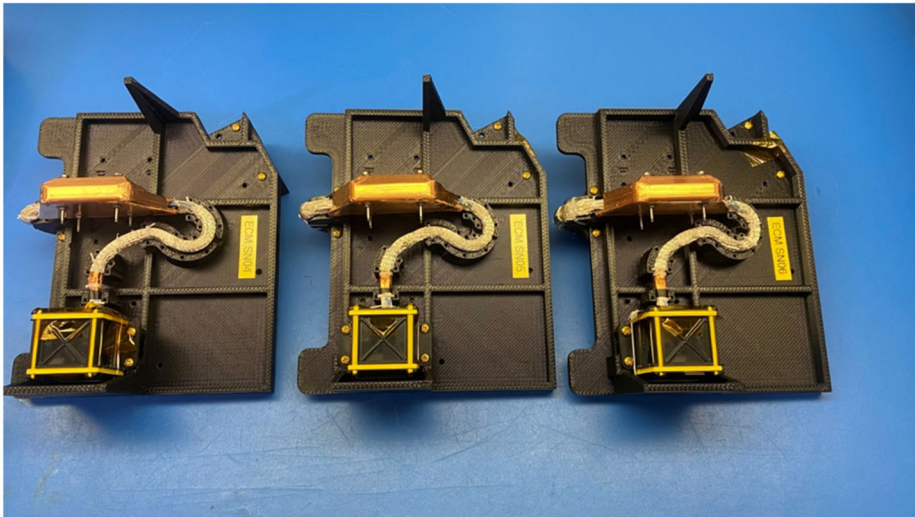


Fig. 7 The three boom sensors in the configuration shown in Fig. 6b. The sensors are integrated with a handling fixture that holds the pigtail in the nominal flight configuration. The pink and yellow unit is the heater pod. The photograph was taken prior to delivery to JPL. Photograph courtesy Christopher Ruiz, NASA/JPL

The sensor head assembly, harness, and heater pod are shown in Fig. 7 mounted in a handling fixture that supports the pigtail in the flight configuration; this configuration is maintained throughout testing, calibration, and integration with the boom. The sensor shield developed by JPL to protect the UCLA sensor head assembly (see Fig. 8) is designed to withstand the Europa Clipper electromagnetic, thermal, launch vibration, mechanical shock, and radiation environments without introducing detectable distortion of the sense signal from any anticipated environment. During prototype development, shielding made from titanium was found to generate a significant magnetic field (tens to hundreds of pT) when the material sustained a thermal gradient. Experiments with titanium and aluminum samples in different shapes and sizes demonstrated that this “thermomagnetic” effect occurred in both metals. (The response was stronger in Ti than in Al.) In order to eliminate the problem of stray fields, all fluxgate sensor shielding and support structure materials were required to be non-metallic and to undergo testing for thermomagnetic susceptibility. Various references provided useful guidance leading to specific design choices (Smith et al. 1975; Acuña 2004; Jager et al. 2016; Grotenhuis et al. 2019; Schnurr et al. 2019). The final material selections of carbon-fiber composite and carbon-filled PEEK satisfied our requirements of high radiation tolerance, low susceptibility to IESD, desirable responses over a wide temperature range, and demonstration of no thermomagnetic effect. Bonded joints and PEEK pins fixed with staked carbon-fiber cross-pins were used instead of metal fasteners within the sensor assembly.

The sensor baseplate and EMI shield carbon-fiber composite material, M55J fibers with RS-3C resin, was selected for its compliance with the aforementioned requirements and also because of its demonstrated attenuation of the REASON emission frequencies (see Sect. 4.2). In order to prevent the electrically-insulative resin from generating IESD impulses, the composite parts were painted with dissipative BR-127 black primer. Silver epoxy, thinly applied onto the edges of the FGS baseplate and EMI shield, connects the ends of the carbon fibers to a common ground path to bleed charge to the pigtail overshield. The heated

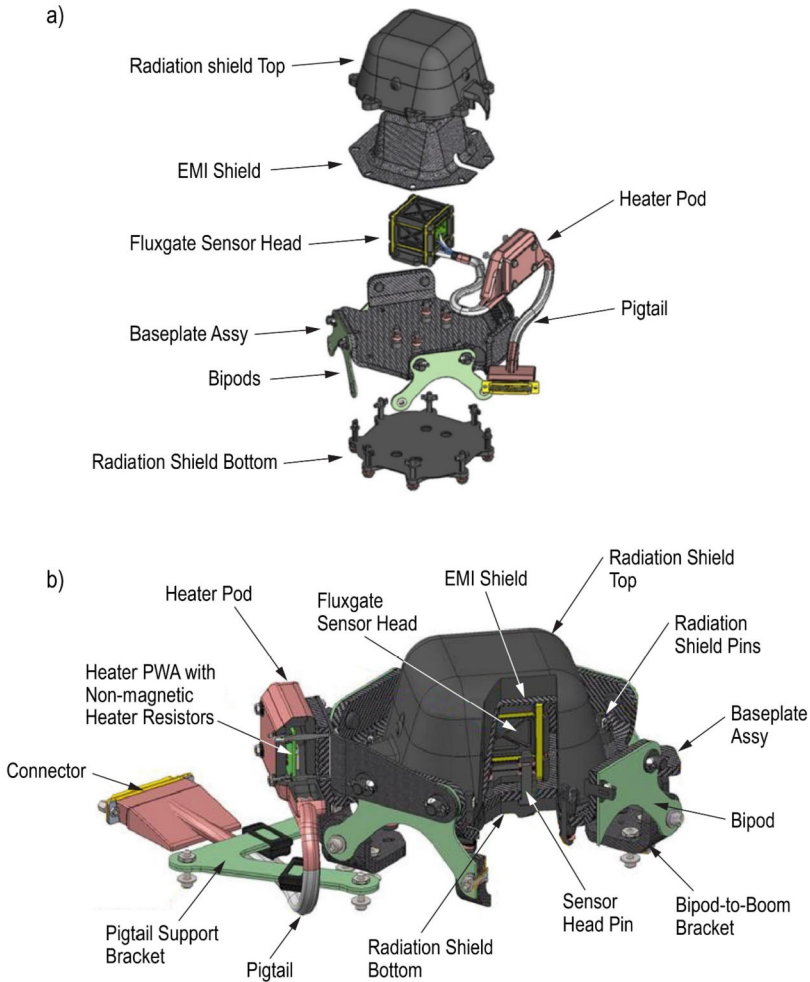


Fig. 8 ECM fluxgate sensor assembly, complete with boom interfacing structure and shield covers. Figure (a) shows an exploded view, while (b) shows the complete sensor assembly in flight configuration, with cutaways to show the heater board inside the heater pod and the fluxgate sensor head inside its shielding

baseplate assembly is thermally isolated from the boom by bipods made from 1/16" G-10 fiberglass, also coated with BR-127 black primer for IESD mitigation.

The radiation shield for the sensor and heater pod, made from the same custom PEEK plastic as the sensor head parts, reduces the interior radiation dose to a level [1-5 Mrad (Si)] survivable by the least-radiation-tolerant materials, which in general are the polymeric and adhesives. PEEK is radiation tolerant to gigarads (Si), but the addition of carbon filler reduces the PEEK's effective bulk volume resistivity from $\sim 5 \times 10^{16} \Omega \text{ cm}$ to $\sim 2 \times 10^{11} \Omega \text{ cm}$, which has been shown by modeling to be sufficiently low to avoid generating harmful IESD events within the FGS assembly.

5.1.2 ECM non-magnetic heater drive circuit

The ECM heater circuit has been specifically designed to dissipate power within the FGS heater assembly in a way that does not interfere with the sensors' ability to measure the local ambient magnetic field. Power dissipation necessarily requires current to flow through the FGS heater element, and currents necessarily produce magnetic fields. The heater circuit was designed to prevent the heating currents from corrupting the magnetic measurement. Several strategies were employed to accomplish this objective.

- 1) The heater current, rather than being delivered through a simple DC (on/off) switch, uses a full bridge circuit such that currents alternately flow in opposite directions with a mean of zero.

- 2) The fundamental frequency chosen for the AC current (~ 47 kHz) avoids electromagnetic interference with the fundamental and its harmonics within ECM and ensures compliance with Europa Clipper's EMC control plan.

- 3) The heater itself is designed to cancel the magnetic field produced by the heater current which flows in opposite senses through superposed loops with very small loop areas.

- 4) Since the heater is driven by an AC signal, it is capacitively coupled to the resistive heater elements to remove any residual DC current.

- 5) To modulate the power of the heater, a sigma-delta variable pulse density method is used to gate the AC current on and off at a frequency that matches the "drive frequency" of the magnetometer (8192 Hz). The sigma-delta technique allows for 16-bit control of heater power at power levels between 25-75%. At powers between 0-25% and 75-100%, the heater circuit reverts to a "bang-bang" mode of operation.

- 6) A proportional-integral (PI) control algorithm is used to allow the heater power to be dynamically controlled to regulate the sensor temperature based on a programmable set-point.

Together these techniques produce a sensor heater system that provides thermal control of each FGS independently, maintaining sensor temperatures to within 1°C of their setpoints with low magnetic emissions while exposed to the variations in thermal environments that they will encounter at Jupiter.

5.2 Electronics

The electronics implement the PRM architecture of the magnetometer (Russell et al. 2016). The EU drives the ring cores in each FGS at a frequency of 8.192 kHz, then receives, filters, and demodulates the FGS second harmonic signals that are proportional in amplitude to the external magnetic field value, and drives the FGS feedback windings to null the external field. This technique ensures that nonlinearities are below ~ 80 dB over the ± 4000 nT measurement range. This functionality is accomplished primarily by two PWAs: the fluxgate (FG) board, which handles analog signal conditioning (amplification, filtering, voltage-to-current conversion), and the FPGA board, which performs the analog-to-digital conversion, integration, demodulation, and anti-alias filtering. The power board accepts and filters the spacecraft bus power flowing to two DC-to-DC converters that provide additional power conditioning to the +28 V input voltage and supply voltages at levels +3.3 V, ± 5 V, and ± 15 V to operate the FPGA and FG circuitry. Three EMI filter boards, one for each set of signals to the three sensors, significantly attenuate any HF and VHF interference that may be picked up by the sensors and cabling.

In addition to handling control and data processing for the PRM, the FPGA board provides the redundant serial interfaces for

- ten distinct instrument commands and telemetry with the spacecraft using standard Universal Asynchronous Receiver-Transmitter Low-Voltage Differential Signaling (UART LVDS),
- pulse-width modulation control of the fluxgate heaters,
- signal conditioning of health and status telemetry, and
- a test port interface to facilitate testing on the ground.

Instrument data processing is completely logic-based and is implemented in a radiation-tolerant FPGA (RTAX4000). The block diagrams of the FPGA and FG boards are shown in Fig. 9. No software is used within the ECM electronics; the FPGA directly processes simple commands to read from and write to registers and responds to the limited set of mandatory Europa Clipper commands (for example to shut down, reset, or pause transmissions, and to receive and synchronize the spacecraft time message) or locally detected instrument faults. Four unique telemetry packet types are generated: The FG telemetry packets contain vector field data for the three fluxgate sensors and 16 housekeeping data channels; a “Register Read” telemetry packet transmits register contents of requested addresses in response to a “Block Register” read command; a metadata packet is sent in response to a “Set AID_BIN” command (the “Set AID_BIN” command instructs the instrument to mark all subsequent telemetry with a given Accountability Identifier); and an ECM health and status packet transmits the remaining housekeeping data channels, operational status, command counters, and fault reporting. Health and status packets are sent at a rate of one sample per second, on detection of a pulse per second (PPS) signal from the Europa Compute Element. FG packets are transmitted at the commanded rate of either one or 16 vector samples per second.

EMI filters attenuate HF and VHF signals from the REASON instrument to limit their noise contribution to voltages representing less than 30 pT. Radiative susceptibility tests demonstrated that this is achievable with 15 dB and 20 dB attenuation in the 8.5–9.5 MHz and 55–65 MHz ranges, respectively. Conversely, radiative emissions tests demonstrated the need for 21 dB attenuation of ECM noise emitted in those bands. Four filters are populated on each EMI filter board, protecting the drive, sense, and feedback signals of the FGS and its temperature sensor. A balanced- π topology is used for the filtering of sense, feedback, and temperature sensor signals. As the drive signal is unbalanced, its filter incorporates a balun to optimize electrical performance. Surface mount components, selected from a pre-defined portfolio of parts screened to be acceptable for the Europa Clipper environments, minimize the area needed to accommodate the filters.

The Power Supply slice, the FG/FPGA slice, and the EMI Filter subassembly are housed in the EU chassis, measuring 270 mm \times 208 mm \times 134 mm (see Fig. 10). The chassis walls are 5 mm thick and provide radiation shielding to reduce the total ionizing dose on the electronic components inside to between 90 and 140 krad(Si) (RDF = 2). The spacecraft avionics vault maintains the EU within the allowable flight temperature range of -20 °C to 50 °C. The EU does not actively control the temperature of the electronics, so to achieve calibrated magnetometer measurements the EU gains and offsets are characterized from -35 C to $+70$ C.

5.3 Magboom

ECM is mounted on a “coilable” lattice truss Magboom with significant space heritage; it was designed and manufactured by Northrop Grumman Space Systems in Goleta, CA, based on the original AEC ABLE Engineering CoilABLE mast design (Bowden and Benton 1993; Pellegrino 2001). Of particular note is the strong heritage of the boom design from booms used for previous missions carrying magnetometers, including Galileo, Cassini, and multiple

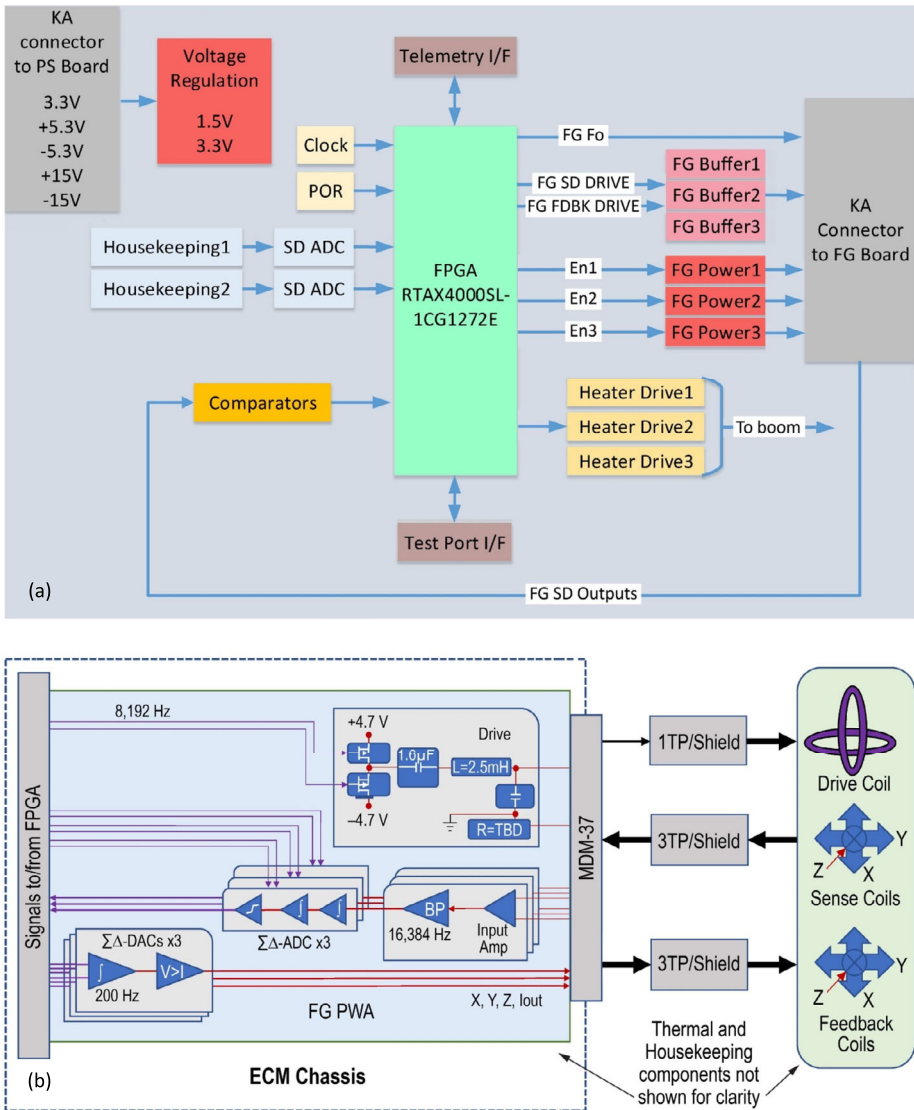


Fig. 9 Block diagrams of the FPGA board (a) and fluxgate board (b). The FPGA implements digital processing of the Pierce-Rowe Magnetometer, spacecraft command and telemetry interfacing, health and status telemetry processing, and FGS thermal control. The FG board amplifies, and filters signals to and from the FGS. Electronics are further described in Sect. 5.2

GOES spacecraft. The continuous-longeron coilable boom provides for compact stowage, ease of operation, and a high stiffness to weight ratio, primarily stemming from its truss geometry and ultra-flexible pultruded fiberglass truss elements (Fig. 11).

In the launch configuration, the boom stows inside its canister (Fig. 12), with triangular battens to control the diameter of the coiled longerons. The canister itself is integrated to the main spacecraft body via an adjustable arrangement of turnbuckle octopod struts, which function both to align the deployment axis and to reduce the thermal conductive losses

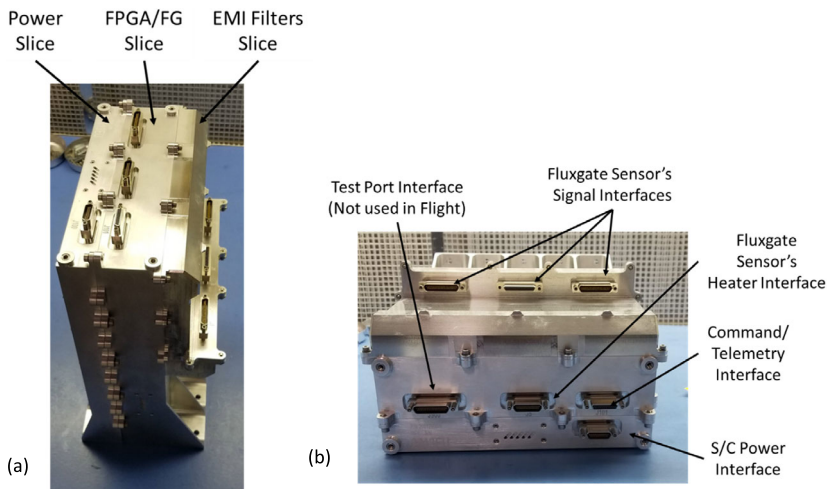


Fig. 10 (a) Photograph of the ECM Electronics Unit, composed of the EMI filters slice, the FPGA/FG slice, and the Power slice and (b) view of the EU's electrical interfaces where spacecraft cable harnesses will mate. The EU is described in detail in Sect. 5.2

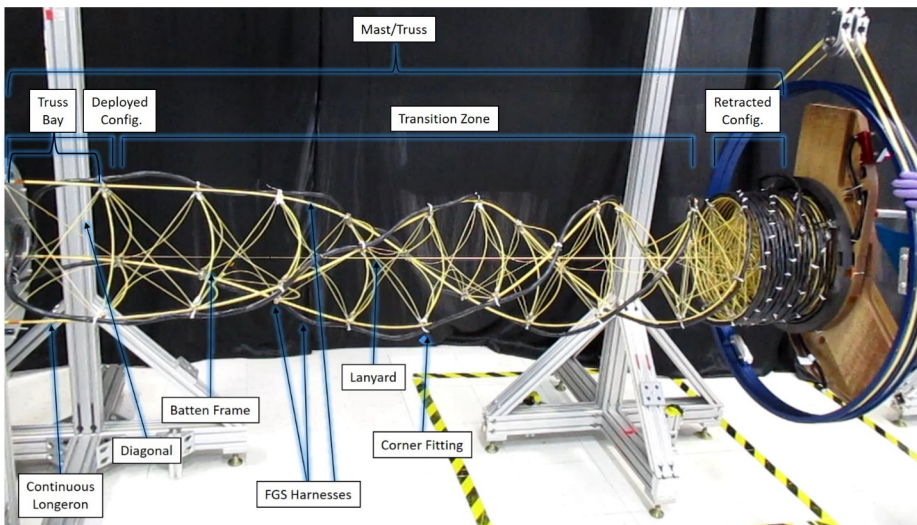


Fig. 11 Coilable Lattice Mast (components defined in the partially deployed example shown here) forms the extendable Magboom structure used to position the fluxgate sensors far from magnetic sources on Europa Clipper. Described in detail in Sect. 5.3

to/from the spacecraft. The three fluxgate sensors are supported by carbon fiber mid-rings mounted along the boom mast and the tip-plate at the end. The tip-plate and mid-rings secure the extendable structure at three tie-down/release mechanisms on the canister while stowed. The load path from the spacecraft to the magnetometers dampens launch loads to a tolerable limit and attenuates the pyroshock load experienced during spacecraft separation from the launch vehicle. The originally specified pyroshock load of 6300 g (at 10,000 Hz) proved

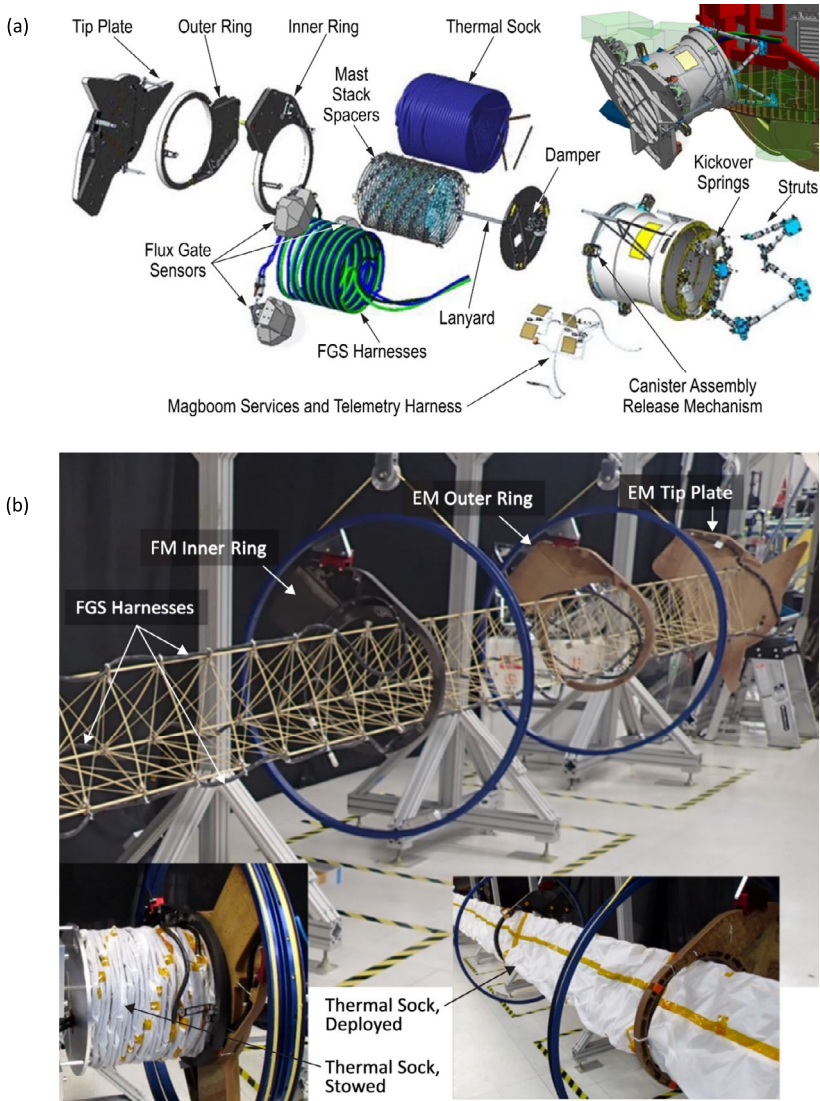


Fig. 12 ECM Magboom configuration. **(a)** Stowed Magboom mounted to the Europa Clipper Propulsion Module. (Middle) Exploded view of the stowed assembly reveals the mast, and FGS support structures and mechanisms. **(b)** The Magboom after it has been deployed. Note how each FGS harness is routed along a dedicated longeron for mass, stiffness, routing, and volume efficiencies. (Bottom Left) Stowed Engineering Model Magboom without Canister, which reveals how the thermal sock is carefully packaged within the canister. (Bottom Right) Deployed Engineering Model Magboom, partial view reveals how the thermal sock encapsulates the mast structure, but not the mid-rings or tip-plate which instead employ optical coatings for thermal control. Separate, static-during-deployment FGS MLI is integrated around each FGS

challenging. The spacecraft-launch vehicle separation mechanism design was subsequently modified and the changes reduced the shock load to <1000 g, a level within the survival capability of the fluxgate sensors.

During early cruise en route to Jupiter, the restraint mechanism will be released via a non-explosive shape memory alloy actuator, allowing the stored strain energy from the coiled mast to initiate deployment. To ensure that the mast erects from the base first (providing a safe and repeatable deployment keep-in-volume) and assist deployment first-motion, three sets of kickover (i.e., “first-motion” or “helper”) springs are employed at the root (base) of each longeron. After release, the stored strain energy within each kickover spring set applies a moment to each longeron root to assist with its 90° rotation erection sequence. During deployment, mast stiffness is thereby established from the base first, with lower stiffness in the transition zone between the erect mast root and the still-stacked and coiled mast at the tip (Fig. 11). Full deployed stiffness is established after each longeron fully straightens, an end-of-deployment sequence that is intentionally dampened to avoid high frequency shock content as the mast reaches full extension. Full deployment is confirmed via microswitches, spatial magnetometer location recovery from science data during the event, and (if needed) in-flight reconstruction of spacecraft mass properties (center of mass, moments of inertia) pre- and post-deployment.

After release, the Magboom completes deployment without support from any external forces (i.e., without a motor or actuator). To ensure a repeatable – but more importantly – *controlled* deployment, a lanyard is attached from the tip plate to a base-mounted rotary friction damper. This passive damper is the sole governor of the deployment rate, whose friction (and therefore internal rotational velocity) is largely dependent on thermal conditions during deployment. An 8:1 gearhead is employed to amplify parasitic torque and reduce the overall impact of temperature on deployment rate. Even so, pre-deployment thermal control is critical to deployment success. The mast must be heated to above $-20\text{ }^{\circ}\text{C}$ to ensure that its harnesses are not too stiff to deploy, and it must not get hotter than $+70\text{ }^{\circ}\text{C}$ to keep the deployment rate safe for the spacecraft. The latter constraint is also critical to maintain while the boom is stowed, where the coilable mast is highly strained and excess heat would eventually delaminate the fiberglass mast and prevent deployment. Once the mast is fully deployed and is relatively unloaded, thermal constraints can be considerably relaxed. The lightly tensioned fiberglass diagonals and intentionally buckled battens provide shear strength and stiffness to each mast bay, the diagonal length designed to control the overall twist and stiffness of the mast. In-flight deployment accuracy, critical for in-flight calibration, has demonstrated uncertainty $<8.5\text{ mrad}$ from deployment to deployment.

As with all elements of ECM, the baseline Magboom design has been tailored for the unique Clipper mission environment while also constraining the quantity and magnitude of design changes to maximize pre-existing flight heritage. Careful consideration was given to IESD, radiation survival, heightened magnetic cleanliness, structural and thermo-mechanical stiffness, near cryogenic mission temperatures, as well as required mass, volume, and pre-existing interface constraints. The most important Magboom design feature for ECM’s experiment is its ability to remain dimensionally stable while experiencing the varying thermal conditions of the European tour. While deployed, departure from dimensional stability is dominated by deflection of the fiberglass mast when exposed to directional thermal loading, primarily from solar radiation, the albedos of Europa and Jupiter, and heat from the spacecraft. Typically, tight thermo-mechanical stability is controlled by either pre-twisting the mast (approximately equalizing the incident solar flux on each longeron) or employing multi-layer insulation over a non-twisted mast (decreasing the solar flux incident on the boom skeleton and splaying the transmitted radiative energy within the insulation). As ECM required the additional deployed stiffness provided by a non-twisted mast, the Magboom has been surrounded with multi-layer insulation configured as a thermal “sock” to maintain thermal stability. This has the added benefit of greatly reducing the radiation exposure and IESD

proclivity of the largely dielectric Magboom mast. Secondary thermo-mechanical stability control is provided by the multi-layer insulation surrounding the titanium canister octopod struts.

5.4 Cables and grounding

The ECM harness set comprises ten cable assemblies: three segments connect each FGS to its vault bulkhead feedthrough (Magboom segment, Propulsion Module segment, and the Avionics Module segment) and a single harness internal to the vault completes the connections from the vault feedthroughs to the Electronics Unit. ECM harnesses consist mainly of TPSJ wires to preserve signal integrity and protect it from interference, and the drive and sense signals to and from the FGS, which are carried on impedance-controlled wire. Connectors near the FGS use non-magnetic materials for contacts, backshells, and fastening hardware and are magnetically screened to ensure that residual fields will not contaminate measurements. Particular care was taken for the inner shields surrounding the individual twisted pairs and overshields encasing the cable bundles for each FGS. To maintain continuity between cable segments, the inner shields pass through the field joints on dedicated pins. The overshields on the In-Vault, Avionics Module, and Propulsion Module segments are formed by wrapping the cable bundle with copper foil, standard for most Europa Clipper spacecraft cables. For ECM's cables on the Magboom, the standard overwrap was shown to induce an interfering magnetic field in the presence of an HF or VHF radiated electric field at levels expected from REASON transmissions. As a result, the Magboom cable segments use a silver-coated copper braid rather than a copper foil wrap over the cable bundles to shield the cables. Because optical coverage of braid overwrap is less than 100%, the Magboom segments are also wrapped with black Kapton to mitigate internal electrostatic discharge.

Shielding and grounding were carefully planned to achieve low noise magnetometer performance. The grounding design is multifaceted and required consideration of the connections of inner shields and overshields, circuit board layouts, subassembly interconnections within the electronics, and conductive paths for all metallic components around the FGS, including elements of the thermal design, to ensure prescribed paths for return currents and to avoid ground current loops. For each FGS, the inner shields for the drive, sense, feedback, and PRT signal lines tie back through HF/VHF EMI filters to dedicated analog secondary-ground planes on the FG PWA in the EU, with each FG channel further separating the drive-signal grounds to better isolate from sense and feedback signals. These individual ground planes connect at a single star ground point on the FPGA board and then to chassis star ground at the ECM power supply. Inner shields for the heater drive signals tie back through dedicated HF/VHF EMI filters to the analog ground for the heater circuits on the FPGA PWA, bypassing the FG circuit board. The overshields are electrically bonded to the connector backshells and to spacecraft ground in order to attenuate electromagnetic interference by creating a Faraday shield. MLI surrounding each FGS connects to the FGS cable's overshield, using a single wire to ensure only one current path to spacecraft ground. Thermal wires, used to transfer heat from the heater pod to the sensors, have no electrical connection to the sensor core but require a ground connection to dissipate IESD. These wires are grounded to the shield of the heater driver signal through a 270 Ω resistor.

5.5 Thermal hardware

The ECM incorporates thermal hardware designed to avoid magnetic contamination while maintaining all elements of the magnetometer within required temperature ranges. The flux-gate assembly heater pod hosts the heater board, which is controlled by the EU as described

in Sect. 5.1. An additional set of magnetically clean heater resistors, powered by the spacecraft instead of the EU when ECM is not operating, is mounted on the heater board to maintain the sensors above their survival temperature of -120 °C. The Europa Clipper spacecraft has allocated 2.8 W power for operational and non-operational heaters at each FGS. While operational, a magnetometer sensor dissipates an additional 350 to 500 mW of power in the fluxgate sense and feedback coils, which helps keep the cores warm (Maghsoudi et al. 2021).

The fluxgate sensor assembly contains four PRTs, one on the printed wiring board on the sensor head (Sensor PRT) and three others on the heater board (Heater PRT). Initially the thermal control system was configured to respond to the Heater PRT, which minimized the lag in temperature response, the temporal variations in the heater power, and, therefore, concerns with control loop instability. During the thermal balance test, this configuration maintained the fluxgate core temperature to within 3 °C of the set point under the worst transient condition expected near closest approach to Europa. Operating with the thermal control system responding to the Sensor PRT was also tested and found to maintain the fluxgate core to within <1 °C of the set point and with acceptable control loop stability and temporal power variations. As a result, the ECM uses the Sensor PRT for control. When the ECM is not operating, the spacecraft monitors the Sensor PRT and energizes the non-operational heaters when the FGS temperature falls below the minimum allowable flight temperature. To reduce radiative heat loss, MLI blankets surround each fluxgate sensor assembly. To reduce conductive heat loss through the mechanical interface between a fluxgate sensor assembly and the Magboom, bipods that support the sensors and the brackets that secure the sensors' pigtail connectors are made from G-10 fiberglass material and titanium, respectively.

Film heaters bonded to the Magboom canister are used to pre-heat the stowed structure and stowed harnesses in preparation for deployment, as described in Sect. 5.2. These heaters are controlled by the spacecraft flight system and provide sufficient heat to raise the temperature of the coiled harnesses above -5 °C to reduce their stiffness and enable successful Magboom deployment. MLI covers the struts at the interface between the canister and the propulsion module and a two-layer thermal sock covers the mast and truss structure to help maintain thermo-mechanical stability. MLI materials underwent tests to verify their ability to survive the Jovian radiation environment and ensure that they present no magnetic contamination.

6 Calibrations and removal of spacecraft stray field

Critical to the achievement of the ECM-related scientific objectives is the measurement stability over the years during which data will be acquired near Europa. Instrument calibration is central to assuring the precision of the measurements. Pre-launch calibrations have been carried out in specialized ground facilities. During both the cruise phase and the orbital phase, in-flight calibrations will track changes, using different approaches appropriate to the environment in which the spacecraft is operating.

6.1 Ground calibrations

The fluxgate magnetometer sensors, in combination with the electronics, exhibit measurement errors in gains (or scale factors), offsets (or zero levels), and alignment (or orthogonality). Gains represent the conversion of the measured analog voltages to physical units of nT.

They depend on the dimensions and number of windings of the sense and feedback coils and on the components of the electronic circuits. The offset of a sensor corresponds to the magnetic field reading in zero field, which is sensitive to such features as the magnetic properties and symmetry of the ferromagnetic core. Alignment refers to the precise orientation of the three sensor axes relative to each other. While these axes are nominally mutually orthogonal, mechanical tolerances and imperfections in the geometry of the feedback coil windings yield deviations from the ideal alignment. These characteristic parameters will vary among sensors and among their axes.

The sensor measurement vector $\mathbf{B}_S = [B_{S1}, B_{S2}, B_{S3}]$ is related to the true magnetic field $\mathbf{B} = [B_x, B_y, B_z]$ through a coupling matrix \mathbf{C} that orthogonalizes and appropriately scales the measurements

$$\mathbf{B} = [\mathbf{C}] \cdot (\mathbf{B}_S - \mathbf{O}) = \begin{bmatrix} B_x \\ B_y \\ B_z \end{bmatrix} = \begin{bmatrix} c_{11} & c_{12} & c_{13} \\ c_{21} & c_{22} & c_{23} \\ c_{31} & c_{32} & c_{33} \end{bmatrix} \begin{bmatrix} B_{S1} - O_1 \\ B_{S2} - O_2 \\ B_{S3} - O_3 \end{bmatrix} \tag{3}$$

(The \mathbf{O} vector for each sensor is the sum of the sensor offset and the component of the DC field of the spacecraft along the sensor axis, as they are not separable.) \mathbf{B}_S and \mathbf{O} are in engineering units (i.e., counts or Volts), \mathbf{B} is in units of nT, and \mathbf{C} is in units of nT/count. Multiplying both sides of the equation with the inverse of the coupling matrix and rearranging yields

$$\mathbf{B}_S = [\mathbf{C}^{-1}] \cdot \mathbf{B} + \mathbf{O} \Rightarrow \begin{bmatrix} B_{S1} \\ B_{S2} \\ B_{S3} \end{bmatrix} = \begin{bmatrix} g_{11} & g_{12} & g_{13} \\ g_{21} & g_{22} & g_{23} \\ g_{31} & g_{32} & g_{33} \end{bmatrix} \begin{bmatrix} B_x \\ B_y \\ B_z \end{bmatrix} + \begin{bmatrix} O_1 \\ O_2 \\ O_3 \end{bmatrix} \tag{4}$$

where \mathbf{C}^{-1} is the orthogonality matrix, which is related to the sensor parameters by the equation

$$[\mathbf{C}^{-1}] = \begin{bmatrix} g_{11} & g_{12} & g_{13} \\ g_{21} & g_{22} & g_{23} \\ g_{31} & g_{32} & g_{33} \end{bmatrix} = \begin{bmatrix} G_1 \sin \vartheta_1 \cos \varphi_1 & G_1 \sin \vartheta_1 \sin \varphi_1 & G_1 \cos \vartheta_1 \\ G_2 \sin \vartheta_2 \cos \varphi_2 & G_2 \sin \vartheta_2 \sin \varphi_2 & G_2 \cos \vartheta_2 \\ G_3 \sin \vartheta_3 \cos \varphi_3 & G_3 \sin \vartheta_3 \sin \varphi_3 & G_3 \cos \vartheta_3 \end{bmatrix} \tag{5}$$

Here, ϑ_i represents the co-latitude of the i -sensor axis relative to the z axis, φ_i represents the azimuthal angle of the projected i -sensor axis into the x - y plane, and G_i is the i -sensor gain. The closer the alignment of the axes is to the orthogonal configuration, the more closely do the coupling matrix and its inverse resemble the identity matrix. The angular relationships are illustrated in Fig. 13.

The gains and alignment of fluxgate magnetometers vary with temperature (assumed uniform across the instrument) because the dimensions of the feedback coils and their relative alignment change slightly as a result of thermal expansion and contraction. In order to ensure accurate and precise measurements, the sensor parameters must be calibrated over a range of operational temperatures prior to integration on the spacecraft with the assumption that changes are predictable within a limited temperature range. These ground calibrations will be used to predict sensor responses, which may vary non-linearly with temperature.

For each FGS, the calibration establishes the relationship between the sensor magnetic axes and its physical reference frame. In a calibration facility, this relationship is established by mounting a “remove-before-flight” fiducial (e.g., rigidly affixed two-sided optical mirror cube) adjacent to each sensor and using a theodolite or an auto-collimated laser beam to measure the physical sensor orientation within the facility. The responses to the calibration

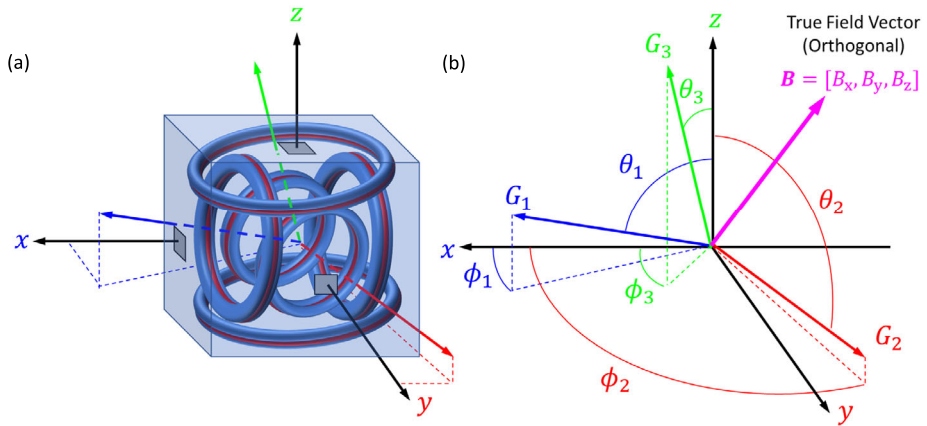


Fig. 13 Exaggerated image illustrating (a) the non-orthogonal reference frame of the sensor (blue, red, green) with respect to the physical reference frame in which the sensor is affixed (black). (b) G_i labels indicate the gains that characterize the slightly different lengths of nominal unit vectors measured by the sensors along the sensor axes color-coded as in (a). Angles are marked to define the notation of equation (5)

field applied by calibration coils of known geometry within the facility are used to establish the relative alignment of the physical and magnetic reference frames. During integration and testing of the flight system, the alignment of the sensors with respect to the spacecraft frame is similarly measured optically. The optical cube is aligned at room temperature; a calibrated magnetic field stimulus is then imposed on the sensor at room temperature and the data are used to establish the differences between optical and magnetic axes. The optical cubes are not used at operational temperatures because the change in sensor response from room temperature to cold temperature is measured with the sensors in a fixed position. For recalibration in flight, stellar reference units will yield the absolute sensor orientation derived from the planned spacecraft rolls.

In order to assure integrity and precision of the scientific results, it is imperative that the calibration parameters of each ECM sensor be well characterized over the operational temperature range and that its alignment with respect to the physical reference frame be determined prior to flight. The Magnetsrode facility of the Technical University of Braunschweig in Braunschweig, Germany was chosen as the facility at which this critical activity could best be undertaken. It is a state-of-the-art facility that provides the tools needed to carry out calibrations over a range of field magnitudes and temperatures relevant to operational conditions at Europa.

The Magnetsrode facility is located in the countryside on the grounds of a federal agricultural research center outside the city of Braunschweig. It consists of several non-magnetic huts located about 35 m apart to isolate calibration operations. There are no man-made structures that generate signals that might interfere with the calibration within a ~ 1 -km radius. Two buildings are of importance to the calibration of the ECM sensor suite: Building 1 hosts the computers for facility control and data acquisition and Building 2 hosts the three-axis calibration coils system with Braunbek configuration (four coils per axis). Furthermore, a reference fluxgate magnetometer, located 50 m away from these buildings and 2 m below ground, monitors Earth's magnetic field as a reference field vector.

The Braunbek coil system has a diameter of 2.5 m and can generate DC and low-frequency AC magnetic fields as large as $\pm 100,000$ nT on each axis (about twice the

magnitude of Earth’s field). Compensation of Earth’s magnetic field is accomplished using real-time measurements from the high-precision fluxgate reference magnetometer. This reference instrument monitors the Earth’s magnetic field and its variations with a resolution better than 0.02 nT. The magnetic field inside the calibration coils can be controlled to 0.8 nT absolute accuracy. A thermal enclosure placed at the center of the coil system enables magnetic field measurements and instrument calibrations in an environment with computer-controlled temperature profiles with temperatures ranging from $-196\text{ }^{\circ}\text{C}$ to $+200\text{ }^{\circ}\text{C}$. The facility is equipped with optical instruments for measuring physical sensor alignment within the calibration coil system. The optical-alignment metrology system in use at the facility can provide an approximate 1 arcmin calibration attitude knowledge, with repeatability of less than 3 arcmin.

The Magnetrode facility was established in 1966 and has been used for calibrating ground- and space-based fluxgate magnetometers, including instruments built by UCLA. Spaceflight magnetometers calibrated at the facility include instruments for the Ørsted, Champ, Deep Space 1, Cluster, Rosetta, Magnetospheric Multiscale (MMS), Solar Orbiter, BepiColombo, JUICE, Comet Interceptor, and Cassini missions. The Ørsted and Champ missions measured Earth’s field from low-Earth orbit and data from these satellites were used to create reference magnetic field models for the Earth between the years 2000 and 2015.

6.2 Removal of the spacecraft magnetic field using gradiometry

The dominant contributions from the spacecraft field to the measurements made by the ECM sensors will be removed from the data of the outboard sensor using magnetic gradiometry. Three three-axis sensors provide nine measurements ($\tilde{\mathbf{B}}_j$ for sensors $j = 1, 2, 3$) along the boom, adequate to establish the dominant properties of the spacecraft field. Three parameters are needed to estimate the ambient field, \mathbf{B}_a , assumed to be uniform across the three sensors; the remaining six parameters can be used to represent the spacecraft field. A spherical harmonic representation through quadrupole order requires eight parameters. However, the six available parameters suffice to estimate the spacecraft magnetic field modeled as a dipole moment \mathbf{M}_{SC} located at a distance r_M from the base of the Magboom. The resulting perturbation at sensor j is given by $\mathbf{B}_{SC,j}$. For this model,

$$\tilde{\mathbf{B}}_j = \mathbf{B}_a + \mathbf{B}_{SC,j} \tag{6}$$

$$\mathbf{B}_{SC,j} = \frac{\mu_0}{4\pi} \frac{3[(\mathbf{r}_j - \mathbf{r}_M) \cdot \mathbf{M}_{SC}](\mathbf{r}_j - \mathbf{r}_M) - \mathbf{M}_{SC} |\mathbf{r}_j - \mathbf{r}_M|^2}{|\mathbf{r}_j - \mathbf{r}_M|^5} \tag{7}$$

Even though the spacecraft produces a highly multipolar field near the base of the boom [there is power at spherical harmonic degrees from $l = 1$ to ∞ (Hurwitz 1960)], in the far field an offset dipole model provides a good approximation to the spacecraft magnetic field at each sensor. One way to solve for the nine parameters contained in the three vectors \mathbf{B}_a , \mathbf{M}_{FS} , and \mathbf{r}_M , is to minimize the following error function,

$$\mathcal{E} = \sum_{j=1}^3 \left| \tilde{\mathbf{B}}_j(\mathbf{B}_a, \mathbf{M}_{SC}, \mathbf{r}_M) - \mathbf{B}_j \right|^2 \tag{8}$$

A non-linear least squares approach is required to solve for these parameters for non-zero values of \mathbf{r}_M . Magnetic sources are widely distributed on the spacecraft (see Fig. 5). Simulations allowing the sources to vary within established limits and to find the location and

properties of an effective dipole moment that could be identified by three magnetometers along the boom showed that it was centered close to the base of the boom (Cochrane et al. [in prep](#)), so the modeled effective field of the spacecraft was placed there. For this approximation, a linear-least squares approach establishes the spacecraft magnetic field at the sensor locations. However, in order to evaluate the SC field for all possible sensor locations along the boom, we solve equation (8) using a constrained non-linear least-squares approach, an approach that sets upper and lower bounds on the parameters of interest. This constrained non-linear estimation problem can be implemented via the Levenberg-Marquardt (Levenberg 1944; Marquardt 1963; Moré 1977) and trust-region-reflective methods (Coleman and Li 1994, 1996).

The precision of the gradiometry method in determining the contributions of the spacecraft field varies with the location of the two movable sensors (inboard and middle). In order to identify optimal sensor locations, we simulated measurements of the ambient and spacecraft magnetic fields for different sensor placements along the boom. For each configuration, we conducted a Monte Carlo simulation using a range of spacecraft magnetic field models consistent with the Europa Clipper multiple dipole model (Sect. 4.3) and allowed for various sensor noise patterns and offsets. In our analysis, we simulated \mathbf{B}_j at sensor j as a superposition of the ambient field, \mathbf{B}_a (assumed to be uniform across the flight system), the SC magnetic field, $\mathbf{B}_{SC,j}$, the sensor and instrument noise, $\mathbf{B}_{n,j}$, and the sensor offset, $\mathbf{B}_{o,j}$. The components of the ambient field were sampled from a uniform distribution in the range ± 500 nT, the noise was randomly sampled from a time-sequence corresponding to electronics white-noise of $50 \text{ pT}/\sqrt{\text{Hz}}$ and sensor flicker-noise ($1/f$ power spectrum) with $100 \text{ pT}/\sqrt{\text{Hz}}$ at 1 Hz, and the offsets were randomly sampled from a uniform distribution in the ranges ± 0.5 and ± 1 nT. We estimated the expected offset knowledge for the ECM sensors from experience with the Analog Fluxgate Magnetometers (AFG) (Russell et al. 2016) of the MMS mission from which the ECM magnetometers derive heritage. Nearly four years of continuous measurements demonstrate that the MMS magnetometers have typical offsets of order ± 10 nT per axis and with a long-term drift rate less than 1 pT/day. If we assume the same performance as that provided by the AFG magnetometers on MMS, then we expect to have offset knowledge well below these values because of two types of planned ECM in-flight calibration activities described in Sect. 6.3. Calibrations to be performed in cruise and during the tour are described in Sects. 6.3 and 6.4, respectively. Assuming a drift rate of 1 pT/day, we expect that even without further calibrations, the offset knowledge should be better than ± 0.9 nT per axis by the end of the four-year nominal mission. In addition, the calibration rolls described in Sect. 6.4 will reduce offset uncertainties to less than ± 0.5 nT per axis.

The RMS error of the inferred ambient field depends on the placement of the inner and middle sensors along the boom as well as spacecraft field offsets, electronics white noise, sensor flicker noise, and sensor offsets. The outboard sensor is fixed at the end of the boom and the positions of the two inner sensors are constrained by mechanical properties of the Magboom. The inner sensors have been placed at allowed positions that optimize estimates of the ambient field. Estimates of the RMS error of the measured field for a range of anticipated noise sources are plotted in Fig. 14 for assumed sensor offsets of ± 0.5 nT (left) and ± 1.0 nT (right). In each figure, a magenta-colored square has been placed at a mechanically allowed location (see Sect. 4.3) near the region of minimum error. For the two assumed offset scenarios, the RMS error in the measured ambient field at the selected locations is 0.42 nT and 0.70 nT and the offsets are characterized to better than ± 0.5 nT.

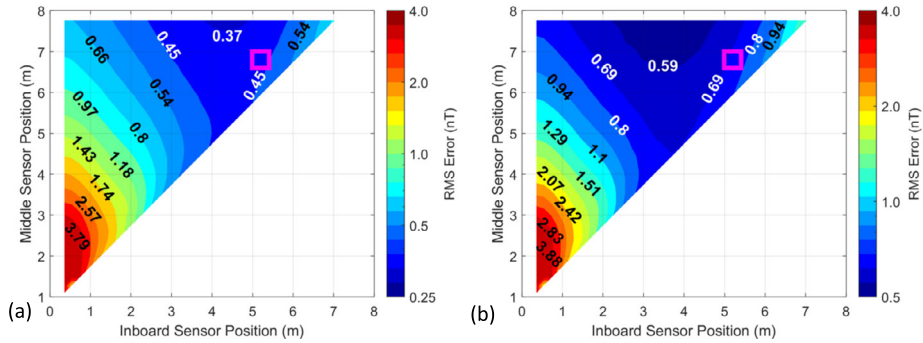


Fig. 14 Logarithmically spaced contour lines representing the RMS error in the inferred ambient magnetic field for different positions of the inboard sensor (abscissa) and middle sensor (ordinate) positions for assumed sensor offsets of (a) ± 0.5 nT and (b) ± 1.0 nT. The magenta squares are placed at the selected positions of the inboard and middle sensors

6.3 In-flight calibration (in the solar wind)

Twelve calibration parameters are needed to fully calibrate the sensor triad; they comprise three offsets, three gains, three orientation angles of the sensor triad and three mutual angles between the sensors. During cruise, we will estimate the sensor offsets by monitoring the interplanetary magnetic field (IMF) (Davis and Smith 1968; Belcher 1973; Leinweber et al. 2008). The approach takes advantage of the fact that the dominant perturbations of the quiet solar wind are Alfvénic. This means that, other than in regions containing interplanetary shocks and sector boundaries, most solar wind magnetic field perturbations are rotations of the field direction with essentially no change of field magnitude. In the presence of an offset, a rotation will change the measured field magnitude. By acquiring time sequences of the ambient field in the quiet solar wind, the sensor offsets, \vec{O}_i , for each of the three magnetometers ($i = 1$ to 3), can be estimated as those values that minimize the variance of the squared magnitude of the measured field $|\mathbf{B}_M|^2$ where $\mathbf{B}_M = (B_x, B_y, B_z)$ (Leinweber et al. 2008). Application of this technique to the calibration of magnetometers on Venus Express (VEX) and on the multiple spacecraft of the Time History of Events and Macroscale Interactions during Substorms (THEMIS) mission produced total offset estimates with uncertainties of better than 0.3 nT.

The first step in this process is to select one or more intervals of magnetometer data extending collectively over at least 8 hours when the spacecraft is in the solar wind and spacecraft field disturbances are minimal (as indicated by housekeeping data and field measurements). This time series is divided into smaller intervals with a prescribed overlap (60 s). The smallest such interval (w_{min}) is determined by the shortest rotation interval expected for the solar wind. Using solar wind observations from the Advanced Composition Explorer (ACE), VEX, and Juno missions, the minimum rotation interval has been found empirically to be ~ 320 s and ~ 480 s at 1 and 3 AU, respectively.

After stepping through the entire data set with the smallest interval, the interval size is incrementally increased by 20% such that $w_1 = w_{min} \times 1.2$ and the calculation of offsets (described below) is repeated until a maximum duration for the intervals, w_{max} (~ 30 minutes at 2 AU), is reached. By stepping through multiple times with increasing interval sizes, rotations with different durations can accurately be captured. Both w_{min} and w_{max} are expected to increase with increasing distance from the Sun. The appropriate w_{min} and w_{max} for approach at Jupiter will be determined based on trending of these parameters in-flight.

For each of the intervals described above, the offsets are calculated individually for each of the three ECM sensors. The processing method is described in detail in Leinweber et al. (2008). In general, the offsets are identified by solving for \mathbf{O} in the equation $[\mathbf{A}] \cdot \mathbf{O} = \mathbf{b}$, where $[\mathbf{A}]$ is the covariance matrix

$$[\mathbf{A}] = \begin{bmatrix} \langle B_x^2 \rangle - \langle B_x \rangle^2 & \langle B_x B_y \rangle - \langle B_x \rangle \langle B_y \rangle & \langle B_x B_z \rangle - \langle B_x \rangle \langle B_z \rangle \\ \langle B_y B_x \rangle - \langle B_y \rangle \langle B_x \rangle & \langle B_y^2 \rangle - \langle B_y \rangle^2 & \langle B_y B_z \rangle - \langle B_y \rangle \langle B_z \rangle \\ \langle B_z B_x \rangle - \langle B_z \rangle \langle B_x \rangle & \langle B_z B_y \rangle - \langle B_z \rangle \langle B_y \rangle & \langle B_z^2 \rangle - \langle B_z \rangle^2 \end{bmatrix} \quad (9)$$

and the angle brackets denote temporal means over the time period. The offset, \mathbf{O} , and \mathbf{b} are defined as

$$\mathbf{O} = \begin{bmatrix} O_x \\ O_y \\ O_z \end{bmatrix} \quad (10)$$

$$\mathbf{b} \equiv \frac{1}{2} \begin{bmatrix} \langle B_x |B_M|^2 \rangle - \langle B_x \rangle \langle |B_M|^2 \rangle \\ \langle B_y |B_M|^2 \rangle - \langle B_y \rangle \langle |B_M|^2 \rangle \\ \langle B_z |B_M|^2 \rangle - \langle B_z \rangle \langle |B_M|^2 \rangle \end{bmatrix}, \quad (11)$$

and B_M is the magnitude of the measured field. We solve for \mathbf{O} using a linear least squares approach. In the above equations, the known (measured) quantities are B_x , B_y , B_z , and B_M .

Since the measured field is a combination of the true ambient field and the offsets we can also write $|B_M|^2 = |B_A|^2 + 2O_x B_x + 2O_y B_y + 2O_z B_z + O_x^2 + O_y^2 + O_z^2$, where $|B_A|^2$ is the true squared magnitude of the IMF (i.e., the measured value corrected for offsets). To check that the offsets are accurate, the estimates for the offsets are subtracted from the measurements to give an estimate of the actual IMF, $\mathbf{B}_A = \mathbf{B}_M - \mathbf{O}$. The slope of $|B_A(t)|^2 - \langle |B_A| \rangle^2$ versus $B_{Ai}^2(t) - \langle B_{Ai} \rangle^2$ will be near zero for each component $i = x, y, z$ if the offsets have been correctly identified. This expresses the fact that for the correct choice of offset, the total field should not change even though individual components will change for a time interval of data recording a pure IMF rotation. Once offsets have been calculated for each interval, the average offset is determined for the entire data set and subtracted from the measured values. The maximum and minimum offset are also identified in order to quantify the uncertainty in the calculation. A final step will check whether the slope of $|B_A|^2(t) - \langle |B_A| \rangle^2$ plotted as a function of $B_{Ai}^2(t) - \langle B_{Ai} \rangle^2$ is linear with zero slope for the time intervals that pass the selection criteria after the average offsets have been subtracted. If these criteria are not met, then the offset calculation must be repeated using different (longer or shorter) time intervals and possibly removing time intervals with large contributions from flight system fields.

6.4 In-flight calibration during the tour

Data acquired in the solar wind are useful for establishing sensor offsets but do not quantify errors introduced by non-orthogonal sensor orientations and mismatched gains. Those parameters, as well as updated offsets, will be determined through the use of calibration rolls after Europa Clipper has entered Jupiter’s magnetosphere and encountered fields of order 200 nT or greater. The method to be used relies on the observation that when the field values measured by sensors on a spacecraft rolling at a fixed period are despun, calibration errors introduce first and second harmonics of the spacecraft roll frequency in the despun magnetic field. Geophysical data should not possess significant signals at the harmonics of the

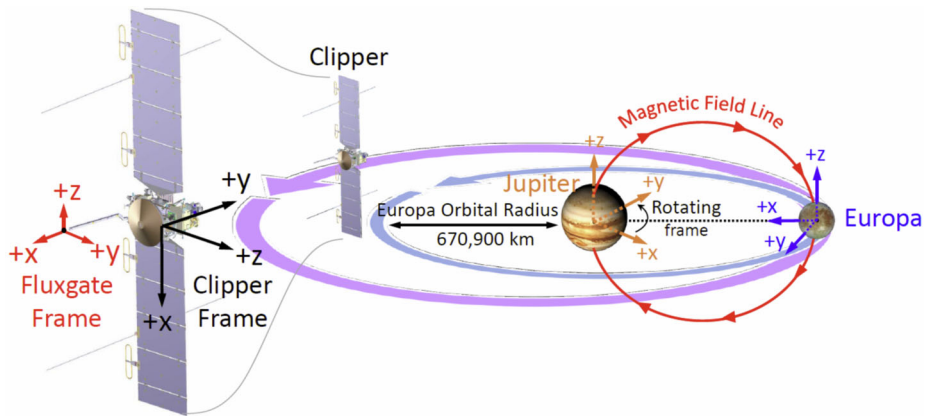


Fig. 15 Relevant reference frames (fluxgate frame in red, spacecraft frame in black, Europa frame in blue, Jupiter SIII in orange) for in-flight calibration roll maneuvers and processing

spacecraft spin period. The amplitudes of the spin tones are proportional to the calibration parameters and for many calibration parameters are also proportional to the strength of the background field (Kepko et al. 1996).

The calibration method calls for the spacecraft to perform a series of rolls at a constant angular rate about at least two approximately orthogonal axes. Assuming that the spacecraft is able to acquire measurements with adequate variation in orientation and magnitude of the background field with respect to the sensor axes, data acquired on rolls about one axis establish 8 of 12 calibration parameters; three additional calibration parameters are established to the required precision from rolls about an approximately orthogonal axis. Thus the method extracts 11 of the 12 calibration parameters for each magnetometer, those chosen to be the 3 offsets, 6 alignment angles, and 2 of 3 gains. The gain of the field measured by a vector magnetometer cannot be determined in flight without an absolute reference. Consequently, the gain of one axis of each sensor triad will be referenced to the absolute gain established during the ground calibration campaign. Analysis of data from spacecraft rolls will then establish the gains for the other two axes of the sensor relative to the gain of the first axis.

The reference frames relevant to the calibration process are depicted in Fig. 15. (Induction analyses adopt a different coordinate frame for Europa.) The data are despun into Jupiter System III coordinates, averaged (by a running average filter with a length equal to or longer than the spin period of the spacecraft) to remove the first and second harmonic spin tones and then respun to the spinning spacecraft frame to obtain the model field, $\mathbf{B}_{\text{model}}$, that provides a good estimate of the environmental field. An iterative least-squares inversion technique is used that compares the successively improved calibrated spacecraft and model field vectors to optimize the calibration parameters until no improvements are obtained in the calibrated parameters. Effectively, the calibration parameters are continually re-estimated, iterating until the spin period signal in the despun data is reduced to an acceptable amplitude.

As mentioned above, the absolute gain factor of the sensor assembly is not established, but it is not needed for the primary objective of ECM science because the success of the induction experiment depends on measuring the ratio of Europa's inductive response and the primary field. The dual-axis roll technique was first implemented on Cassini Grand Finale orbits (Cao et al. 2020). The spacecraft executed 6 rolls in approximately two hours during each of the calibration maneuvers performed. The procedure provided calibrated data

with an accuracy better than 2 nT in a background field of 20,000 nT present near closest approach.

A least-squares approach extracts calibration parameters that depend on the amplitudes of the magnetic signatures that vary at the spacecraft roll frequency and its second harmonic. It is, therefore, critical that the data acquired for processing include multiple full 360° rolls. Six spacecraft rolls about each of two axes were found to suffice for calibration when spinning the flight system at 0.04°/sec (2.49 h/revolution, the fastest rate allowed for this spin axis) about the spacecraft *Y*-axis and 0.057°/sec (1.75 h/revolution) about the spacecraft *X*-axis. (The spacecraft can spin as fast as 0.096°/sec or 1.04 h/revolution about the spacecraft *X*-axis, which is parallel to the solar panel's long axis.)

The orthogonality and gain parameters are extracted from the amplitude of the second harmonic, which is proportional to the ambient field strength. Consequently, a full calibration requires that the rolls be executed where the field strength is sufficiently large (>200 nT, a level reached within $\sim 15 R_J$ of Jupiter) to impose a clear signal. In the planned mission tours, calibration rolls are incorporated on both inbound and outbound legs of the Europa flybys (each around a different axis) on every second or third Jovian orbit depending on the number of Europa orbits between encounters. In a few cases, the rolls are inbound on one orbit and outbound on the next orbit, meaning that one of the rolls is separated by only two orbits from the closest calibration roll. End to end simulations using realistic field models (e.g., Khurana 1997) and assuming typical tours with of order forty flybys show that a precision of 1 nT can be achieved in observations using this scheme.

7 Operations, data processing and archiving

The nominal operation of the Clipper magnetometer is straightforward. Once powered on and configured, instrument commanding consists mostly of changing data rates and assigning unique data accountability identifiers (AIDs) and downlink priorities to various science and calibration activities. After the data are acquired and returned to Earth, they are processed at the ECM Science Operations Center (SOC) and made available for analysis by the ECM Science Team. The SOC also prepares data for sharing within the Europa Clipper Science Team and archives them with the Planetary Data System (PDS). This section discusses the details of each of these aspects of operating the instrument.

7.1 Instrument commanding and modes

The ECM instrument has 3 main operational modes: OFF, IDLE, and MEASUREMENT as shown in the mode transition diagram (Fig. 16). The ECM instrument is also capable of running 6 in-flight test modes (sub-modes of MEASUREMENT) for diagnostic purposes. When ECM is OFF, there is no power to the instrument and non-operational control of the fluxgate heaters is provided by the spacecraft in survival mode.

As previously described, the ECM Instrument controller is a one-time programmable RTAX FPGA in the ECM Flight Electronics Unit. Upon power on (MAG_POWER_ON), control of the fluxgate heaters is transferred to ECM and the instrument is configured using default values programmed prior to delivery to the spacecraft for integration. ECM begins generating health and status (H&S) data but the fluxgate sensors remain powered off; this is called the IDLE mode. The ECM configuration is then updated to the best available FG tuning, heater control, and fault protection configuration parameters by sending an instrument command file. A set of ECM command files, including a “standard configuration file” are

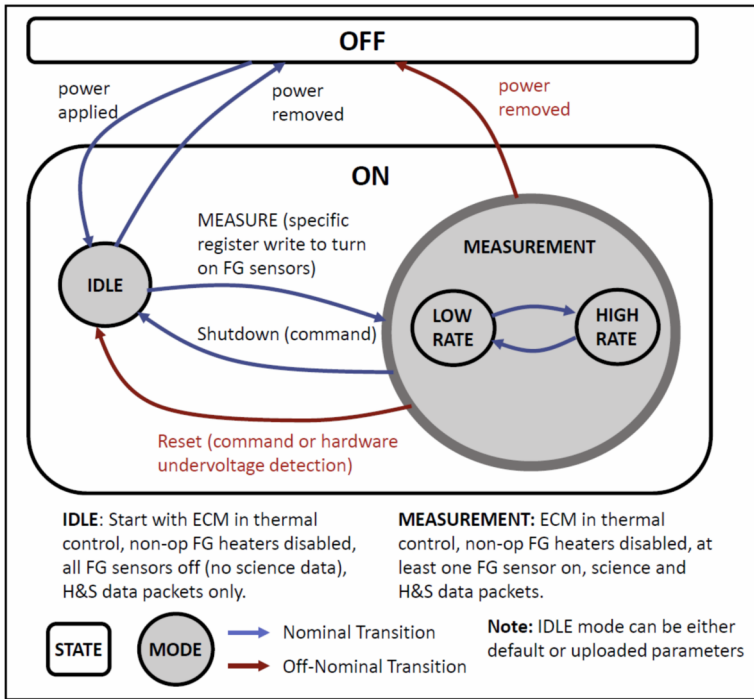


Fig. 16 ECM mode transition diagram

stored on the spacecraft. These files are created on the ground and then sent to the spacecraft where they can be used as needed by instrument command sequences. Command files contain a set of low-level instrument commands, which the spacecraft sends to the instrument sequentially at a rate of one command per second to write and read FPGA registers. The nominal ECM configuration has all three fluxgate sensors powered on but the instrument is considered to be in MEASUREMENT mode when any one of the fluxgates is powered on. The FGS can be powered on by the commands in the configuration command file or by using the MAG_MEASURE command. Once in MEASUREMENT mode, the instrument begins generating science data packets. The ECM operates at two science data rates: a 16 sample per second (sps) high rate and a one sps low rate. The instrument sample rate can be set in a configuration file or by using the using the MAG_RATE command with an appropriate parameter (HIGH_RATE, LOW_RATE).

The ECM will normally be powered on and configured by using the MAG_DO_SCIENCE behavior that includes a configuration command file parameter. A behavior is a set of pre-defined commands, such as the MAG_POWER_ON behavior. The MAG_DO_SCIENCE behavior first powers on the instrument and then loads a configuration file. When the MAG_DO_SCIENCE behavior load completes, the instrument is fully configured and in MEASUREMENT mode at the rate specified by the command file. The ECM is powered on continuously during Jovian tour operations but will be powered off for most of the interplanetary cruise except for the boom deployment and calibration activities. When ECM is powered off (MAG_POWER_OFF), the instrument performs an orderly shutdown by first powering down the FGS, then removing power from the instrument and reasserting spacecraft control of the fluxgate heaters in survival mode. A special configuration file is used

Table 4 ECM high level commands

ECM FSW Behavior/Commands	Description/Use Case
MAG_POWER_ON	Nominal Power On set of commands that assert ECM control over the fluxgate heaters without powering on the fluxgates. ECM is in the IDLE mode upon completion.
MAG_SEND_CMD_FILE (file)	Used by spacecraft to send a set of low-level instrument commands (FPGA register reads and writes) one at a time to the ECM instrument. The commands are stored in a file that is uplinked to the spacecraft and stored in spacecraft memory to be used as needed.
MAG_DO_SCIENCE (file)	Executes a set of commands that are sent in the following order: MAG_POWER_ON, MAG_SEND_CMD_FILE, MAG_MEASURE. Upon completion of this command, the ECM Instrument is placed into MEASUREMENT mode.
MAG_MEASURE	Commands to power on the fluxgates putting ECM into MEASUREMENT mode
MAG_RATE (rate)	Command sets ECM into high-rate or low-rate mode depending upon the argument provided.
MAG_SHUTDOWN	Commands to power down the fluxgates leaving ECM in IDLE mode
MAG_POWER_OFF	Nominal Power Off command that turns the instrument off and places the spacecraft in control of the fluxgate heaters (non-operational control).

to command an engineering mode that samples at 128 sps if needed to analyze operational anomalies. The complete set of high-level ECM commands and behaviors is provided in Table 4.

The ECM has an internal fault monitoring system referred to as the Fault Response Management System (FRMS). This system can be configured to detect internal faults and can request action from the spacecraft via the ECM H&S Packet (returned to the spacecraft once per second). Depending upon the nature of the fault, ECM is capable of requesting either an immediate power off or a power cycle/return to science (MAG_DO_SCIENCE). The ECM FRMS monitors 26 internal health and status channels (currents, voltages, and temperatures). The FRMS can request that the spacecraft power off or power cycle the instrument or it can autonomously shut down any single fluxgate if a fault is detected. The instrument configuration command file loaded after power on configures the FRMS as well as the fluxgates.

The ECM can also be configured to operate in six different test modes. Test mode data returned in science data packets will make it possible to diagnose anomalous ECM behavior after launch.

7.2 Cruise operations

Most first-time activities for the spacecraft and payload will take place early in the cruise phase during two periods referred to as Flight System Characterization Part 1 (FSC1) and Part 2 (FSC2). FSC1 will comprise the activities that must be done prior to the execution of the first trajectory correction maneuver (TCM-1) and does not include any ECM activities. FSC2 begins about two weeks after launch and it includes the deployments of both the ECM Magboom and the REASON antennas. The first step for ECM prior to deployment is the aliveness verification activity that will verify that the electronics unit survived launch prior to deployment. This activity powers ECM on for about 10 minutes and will verify that H&S

packets have been created and transmitted to the Deep Space network (DSN); then ECM will power off. The next step in preparation for deployment is pre-deployment heating of the Magboom canister to a temperature at which it is safe to deploy the boom. Heating will take approximately eight hours. In order to ensure that the canister can attain a high enough temperature for deployment with the power available, the boom deployment must take place near 1 AU. This requirement is driven entirely by the heat that can be provided to the canister by solar flux, which becomes insufficient significantly beyond ~ 1 AU. Once heating is verified on the ground, ECM will be turned on and data will be taken on all three magnetometers while the boom deploys. Deployment will be confirmed in real-time by monitoring the state of a pair of microswitches that toggle when the boom begins deploying and again when the full transit is reached. The magnetometer data acquired as the boom unwinds can establish the number of rotations of each sensor and will provide an additional, independent mechanism to confirm full deployment of the boom. Once deployment is confirmed, a post-deployment checkout of the instrument will exercise all of the ECM commands, behaviors, and test-modes. After the initial checkout and REASON antenna deployment, ECM will remain on during FSC2 when possible, taking data on all three sensors as other instruments are checked out. These preliminary data will be used to detect magnetic interference from operation of other instruments and will provide input to a much more extensive interference check to be performed during outer cruise. Nominally, ECM will be powered off after FSC2 (launch + 30 days) and will subsequently operate intermittently for sensor calibration.

Magnetic background calibrations will be performed at a regular cadence in order to monitor offset stability, temperature dependence, and sensitivity to changes in the spacecraft magnetic field. Each instance of the background calibration activity will collect low-rate data from all three sensors for about ten days. The activity will occur twice during the inner cruise phase (once shortly after FSC2 and once near Mars aphelion), and then at a regular cadence during the outer cruise phase – every 3 months starting after the Earth flyby and continuing until Jupiter approach. The last occurrence will be just prior to the start of the Jupiter approach phase at a joviocentric range greater than 300 Jupiter radii.

The Mars-Earth Gravity Assist (MEGA) trajectory features a single Earth flyby during the inner cruise phase, presenting the only opportunity of the mission for an absolute sensor gain calibration in the known field of Earth's magnetosphere. During the Earth flyby (closest approach altitude just slightly more than 3000 km), the ECM will take data with all three sensors in high-rate mode during an interval approximately 30 hours long, centered on Earth closest approach.

During the cruise phase, the ECM will try to characterize the measured disturbance field produced by the spacecraft and its science instruments more thoroughly than possible on the ground. A group of activities to assess potential mutual electromagnetic interferences between instruments, especially between ECM and REASON, will occur during outer cruise (EMI/EMC test). During the ECM portion of these tests, key spacecraft subsystems and instruments will be turned on and operated in various modes while ECM collects data in high-rate mode. These tests will be repeated several times in order to separate spacecraft interference effects from potential changes in the background resulting from IMF fluctuations. The focus will be on specific subsystems and instruments that have been identified as potential noise sources for ECM. The goal is to refine the spacecraft field model to identify the noise that might otherwise negatively impact the interpretation of the flyby measurements critical to the scientific objectives of the mission.

7.3 Science tour operations

During the tour phase, the ECM will take data continuously with all three FGS. During flybys of the Galilean satellites (Europa, Ganymede, and Callisto) and when the spacecraft is within ± 2 hours of closest approach (range approximately 18 Europa radii), the ECM will collect flyby data in its high-rate mode. The ECM will revert to low-rate mode to collect background data between encounters.

In-flight calibration rolls, needed to determine changes in the offsets, gains, and sensor alignments, will be performed approximately every three orbits during the tour phase. Details of this activity are provided in Sect. 6.4. The frequency of roll-calibration events is determined by the calibration stability of the fluxgate sensors, which are expected to remain within allowable stability limits for up to about six weeks. There are some orbits on which the spacecraft energy margins are such that rolls about two orthogonal spacecraft axes cannot both be executed during the same encounter, or fewer than six rolls can be performed about an axis. In these instances, the calibration rolls will be split over consecutive orbits. The ECM science team plans to exercise this dual roll approach on both the inbound and outbound portions of one of the Ganymede flybys early in the tour to check post-launch gains and mutual angles and to validate the calibration roll activity.

All of the Jovian tours currently under consideration include orbits on which the Clipper spacecraft goes into Europa or Jupiter eclipse and spacecraft temperatures fall quite rapidly. The design of the operational heaters for the sensors minimizes and controls the thermal variations within the fluxgate sensors. We do not anticipate the need to adjust the heater settings during eclipses to keep the sensors within a degree or two of normal operating temperatures. However, close attention will be paid to the thermal state of the sensors during the first few eclipses to verify that the heaters are performing as expected.

All data on the Europa Clipper are prioritized for downlink using the following scheme: 1) *decisional* – these data (up to 12.4 Gb) must be returned within five days of an encounter so that they can be used in tuning instrument observations for the next flyby; this category is not relevant to ECM because its operations do not require decisional data for next orbit planning. 2) *this encounter* – data must be returned before the next encounter; 3) *mission* – data must be returned before the end of mission; and 4) *opportunistic* – data should be returned if resources permit. Each of these main categories is further subdivided so that selected small datasets are returned before the larger ones. The ECM has implemented only two of these data priorities. All ECM science and calibration data are assigned to the “*this encounter*” priority bin. ECM encounter data will be downlinked only after the decisional data have been returned. The “*opportunistic*” data priority was implemented in case an unforeseen observation opportunity presents itself during the tour. Other than that, the only anticipated use of the *opportunistic* data priority is during some of the cruise EMI/EMC calibrations when other instruments (REASON, etc.) are observing the impact of different ECM states on their data quality. Data acquired during these calibrations will not be used for ECM science or calibration.

7.4 Science Operations Center (SOC)

The ECM SOC is responsible for both the uplink (planning, sequencing, and review) and downlink (health and status, data processing, calibration, distribution, and archive) aspects of instrument operations. The SOC staff will use JPL multi-mission tools for planning and sequencing and UCLA heritage tools for monitoring the instrument health and status monitoring and processing the science data.

7.4.1 Uplink processes

The ECM SOC will not develop any specialized software or processes to support mission planning and sequencing. ECM is completely dependent on the multi-mission planning and sequencing tools provided by JPL. The nominal operation of the instrument is straightforward, and the tools and processes developed for the mission planning and sequencing teams will be used to plan ECM operations. The *Merlin* planning tool allows users to define a set of reusable types of activities (e.g., calibration rolls) that will be used intermittently during operations. Each activity type includes a set of parameters that vary each time the activity is used (i.e., start/stop time, number of rolls, etc.) and must be provided by the operator each time a specific instance of an activity is requested. *Merlin* activity-type definitions include the information required to expand the activity into the spacecraft and instrument commands required to perform the activity. The activity type definitions also contain information on the power required to perform each activity and the data volume each activity generates. These items are required to support the resource usage modeling component of the mission planning effort. The *Falcon* tool will primarily be used by the JPL sequencing team to integrate, model, and check adherence to flight rules of all of the different components of each two-orbit background sequence and mini-sequences. The ECM SOC staff will review the *Falcon* output to verify that all expected ECM activities are included and that there are no conflicts or rule violations that require the ECM team to change its planned activities.

7.4.2 Downlink processes

Except for a few hours during the deployment of the magnetometer boom, there are no real-time operations associated with the ECM downlink processes. Science and instrument H&S data are stored on the spacecraft and returned to Earth with delays that depend on the data priority and available downlink bandwidth. The ECM data that are returned from the spacecraft are converted from raw telemetry packets into time-ordered ASCII tables by the Ground Data System (GDS) before being delivered to the ECM science team via the *DataDrive* system. *DataDrive* is a file sharing system that will be used by the Europa Clipper Project to exchange data between system elements and science investigations. The GDS provides separate files for the ECM H&S data and the science data from each individual FGS. Upon receipt of data, the first priority of the ECM operations staff is to determine the instrument health and status, and report the findings to the ECM Principal Investigator and the Europa Clipper Operations Lead. Standardized reports will be generated and sent by e-mail to the team leads and placed on *DataDrive* for wider distribution. Reduced rate H&S data will be combined with instrument calibration information to support long-term trending analysis.

7.5 Data processing, data products and archiving

7.5.1 Data processing pipeline

ECM science data are processed using the Data Flow System (DFS) tool initially developed by the UCLA space physics group in 1984. This system is modular and new elements are easy to add at any time. The DFS works on the UNIX principle of piping data between processes. The ECM data processing pipeline will make use of existing modules for reading in, merging, manipulating, and writing data files. Specialized modules that apply the time- and temperature-dependent calibrations for each individual fluxgate will need to be created

either from scratch or by modifying similar modules that were used by the Galileo and InSight magnetometer data processing pipelines. This module will apply the best available calibration (orthogonalization matrix, gains, offsets, and scale factors) to the data for each individual fluxgate sensor. The initial calibration will be the ground calibration. Later in the mission, in-flight calibrations determined by using data from the cruise background field observations (offsets only), the Earth flyby, and the Jupiter calibration rolls will be applied to the data from each sensor. The gradiometer technique will be used to remove spacecraft sources of magnetic interference from the outboard sensor data. Data will be transformed using the SPICE toolkit, which is a combination of software and data (kernels). The toolkit allows users to perform orbit and attitude calculations (Acton 1996) and rotate the data into various reference frames to support a variety of different analyses. The output of the data processing pipeline will be a combination of simple ASCII tables and Common Data Format (CDF) files. The CDF format will be especially useful for correlative analysis of ECM and PIMS data.

7.5.2 Data products

Data will be generated and archived at three different data processing levels: raw, calibrated, and derived. The raw data provided to the ECM team by the GDS team is the lowest data processing level that will be available to the ECM Science team and archived with the PDS. The raw data are stored in comma separated value ASCII files with each record containing an instrument clock value (iSCLK), an uncorrected UTC time value derived from the iSCLK value using SPICE, and a magnetic field vector in raw 24-bit signed integer data number values. The last record from each original telemetry packet will also contain the 16 FGS housekeeping parameters and temperature for each FGS along with health and status data from the EU. These fields will not be included in the other records in the raw data files. Instead, the missing housekeeping values will be indicated by using a set of 16 consecutive commas. The 16 sps FG data include FG engineering values once every ten seconds (160 vectors), and the 1 sps data include such values once a minute (60 vectors). There will be one file per fluxgate for each data downlink session that includes ECM data. Data will be provided in the sensor frame. In addition, there will be an ASCII H&S data file with values in physical units (degrees, amps, etc.) once every minute.

The data from each FGS will be calibrated using the best calibration available for that individual sensor to generate the partially processed data set. This calibration will not include the removal of all of the offsets resulting from spacecraft sources. One high-rate and one low-rate data file will be provided for each sensor and orbit. Data will be provided at full time resolution in the spacecraft bus, boom-aligned frames as well as in geophysical reference frames, and any drift in the instrument clock will be corrected. Orbital data will include relevant information in the Jupiter System III (low-rate orbital) and IAU Europa, Ganymede, and Callisto (high-rate orbital) frames, while cruise data will include information in the Heliocentric radial, tangential, normal (RTN) frame and, for the Earth flyby data, in the Geocentric Solar Ecliptic and Magnetospheric frames (Russell 1971).

The calibrated data from each of the three sensors will be analyzed to remove the spacecraft field source of offset and provide a single estimate of the derived magnetic field. Files containing the most complete possible coverage of the tour will fill into the low-rate data (1 sps) all high-rate data averaged down to a rate of one sps. These data will be provided in the Jupiter System III (1965) reference frame, along with spacecraft position data in the same frame. The high-rate data for each encounter will be provided at full time resolution in several Moon-centered reference frames including IAU Europa, Ganymede and Callisto,

and a co-rotationally aligned frame centered at each moon. Additional frames may be included if they are found to be useful. Spacecraft position data in each reference frame will be provided in a separate file at the tour sampling rate (1 sps).

All archive data products will be generated using the best reconstructed SPICE kernels available 45 days before the PDS release date. The reference frames used will all be defined in a SPICE frames kernel so that the transformations can be unambiguously reproduced by users.

7.5.3 PDS archive

All of the data generated by the ECM investigation will be archived with the PDS using the PDS4 (PDS 2021 or later) standards. The data archive schedule and the rules governing the internal sharing of data within the project are defined in the Europa Clipper Science Data Management Plan (SDMP)¹ (Korth and Paczkowski 2022). The first archive release of flight data will occur six months after Jupiter Orbit Insertion (JOI) with subsequent releases occurring every six months following the time of the first Europa encounter. The ECM data will be organized into a single data bundle (logical identifier: urn:nasa:pds:clipper.ecm) that will contain separate data collections for each data processing level, an ancillary data collection that will include the H&S data, a document collection, and a browse collection of data plots. The ECM Software Interface Specification (SIS) document provides detailed structure of the PDS archive and the magnetometer data processing. The SIS, calibration document, and a data user's guide will be included in the document collection of the PDS archive. Instrument calibration and data processing pipeline software will be archived in the NASA GitHub site.

8 Data analysis and interpretation

8.1 Methods and procedures to retrieve induction signal: Iterative magnetic inversion and a Bayesian approach

8.1.1 Retrieving the induction signal through iterative magnetic inversion

The magnetic field observed near Europa can be written as the sum of an external uniform field and the dipolar response from Europa's ocean, $\mathbf{M}(t)$, and contributions from the moon/plasma interaction field, which is discussed in Sect. 8.2. In the absence of plasma sources, the field takes the form

$$\mathbf{B}_{\text{obs}}(t) = \mathbf{B}_{\text{ext}}(t) + [\mathbf{D}] \cdot \mathbf{M}(t), \quad (12)$$

where the matrix $[\mathbf{D}]$ is composed of elements that depend only on the location of Clipper relative to Europa (x, y, z) at distance r from the center:

$$[\mathbf{D}] = r^{-5} \begin{bmatrix} 3x^2 - r^2 & 3xy & 3xz \\ 3xy & 3y^2 - r^2 & 3yz \\ 3xz & 3yz & 3z^2 - r^2 \end{bmatrix}. \quad (13)$$

¹This SDMP and the archive SIS documents will be assigned DOIs and archived by the PDS in the first data release.

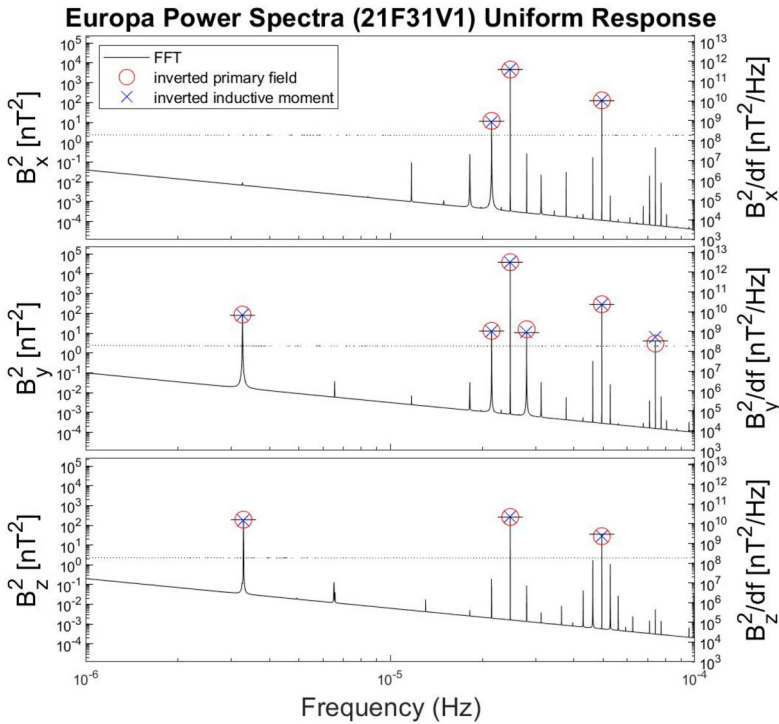


Fig. 17 The power spectrum of the field observed by Europa (solid black lines) calculated from the Jovian field model of Khurana and Tsyganenko (2002) with addition of background noise with total power (50,100,20) nT² in (B_r^2 , B_θ^2 , B_ϕ^2) and frequency variation $\propto f^{-3/2}$, assuming that data were acquired on a nominal set of mission encounters similar to the one finally selected. The value of the power in the three components is highlighted at the six prime harmonics with black horizontal bars (input primary and secondary field). For this simulation, we used the mission tour version 21F31V1, assumed 100% response from Europa’s ocean and did not include plasma noise. The red circles show the power obtained in the inverted primary field and the blue crosses show the power in the inverted inductive moments at the surface of Europa at the pole of the induced dipole moment. The small separations between the crosses and black horizontal bars indicate a highly successful retrieval of the induced dipole moment

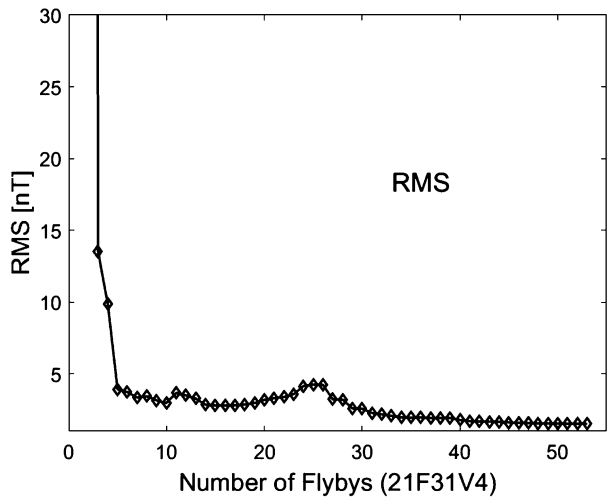
We allow for a fixed dipole moment as well as the induced moment and further assume that both the external field and the induced dipole moment can be decomposed into a DC contribution and contributions at several AC frequencies. A Fourier transform of the external field at the location of Europa shows that only six of the harmonics have wave power larger than 2 nT² (see Fig. 17). Thus, including the DC contribution, the external and internal field in equation (13) are well characterized with seven harmonics:

$$\mathbf{B}_{\text{ext}}(t) = \sum_j \mathbf{B}_{\text{ext}}(\omega_j) e^{-i\omega_j t} \tag{14}$$

$$\mathbf{M}(t) = \sum_j \mathbf{M}(\omega_j) e^{-i\omega_j t} \tag{15}$$

where $j = 1-7$. The time-varying contributions must be represented by both amplitude and phase, so we must determine a total of 78 coefficients from the inversion of equation (13)

Fig. 18 The RMS difference between the input field and the six-frequency-modeled field for the 21F31V1 tour plotted against the number of flybys used in the inversion. A precision of ~ 1 nT is achieved after data from the first 40 flybys are included in the inversion



using all of the flyby data. We use a least squares inversion method to derive these coefficients.

By ensuring that the multiple flybys in the Europa Clipper tour occur for a diverse range of phases of the prime frequencies needed to probe Europa’s interior, we have established that it will be possible to separate Europa’s inductive field from Jupiter’s external field using the intermittent magnetic field measurements obtained near Europa. We tested the method using simulated data that would be acquired during candidate tours developed by the Europa Clipper Project, adding random noise and assuming that the conducting layer extends to the surface and that Europa is a perfect conductor. (In the parameter range of interest, the amplitude of an inductive response changes by a few percent as the conductivity changes by an order of magnitude as can be inferred from Fig. 1b.) We achieved an uncertainty of <1 nT in the RMS error of the amplitudes of the inverted harmonics. Figure 17 shows the results of the inversion for the 21F31V1 tour. In this initial analysis, the effects of plasma noise were ignored.

In further tests, input data extracted from a model of the Jovian magnetospheric field plus inductive responses and modeled plasma noise (see Sect. 8.2) were sampled, again using a realistic tour (i.e., adopting specified encounter phases and European latitudes, longitudes, and altitudes of closest approach). Retrieval of the inductive field parameters improves as the number of close passes increases as illustrated in Fig. 18. The figure shows the RMS errors of the inferred values as a function of the number of close encounters with Europa for a typical tour. Here the RMS error is defined as

$$RMS = \sqrt{\sum_{i=1}^N \sum_{k=x,y,z} [B_{k, input}(i) - B_{k, inverted}(i)]^2 / 3N} \tag{16}$$

The first summation is over the components of the vector field and the second summation is over the number of data used for analysis. Reduction of the RMS error to ~ 1 nT requires roughly 40 close encounters. In all of the tests, the input properties of the ocean and ice layer were recovered within the desired uncertainty well before the fortieth orbit around Jupiter. This technique is quite insensitive to environmental noise unless that noise is strongly modulated at the key natural frequencies, a situation that appears improbable.

8.1.2 Retrieving the induction signal using Bayesian inference

The parameters of Europa's ocean can also be extracted using the approach of Bayesian inference (Biersteker et al. 2021, 2023). This method (1) directly recovers the ocean parameters from the magnetometry; (2) yields robust confidence intervals for retrieved parameters, including uncertainties arising from the non-uniqueness of the solution; and (3) can accommodate constraints from prior observations of Europa and complementary measurements from other Europa Clipper instruments.

In this approach, the ocean is characterized by fitting a statistical model to the magnetic data. The parameters of the model are described by probability distributions representing our initial (prior) knowledge of their values. New observations from Europa Clipper are combined with the prior observations to yield posterior probability distributions for the model parameters. The retrieval model has three components. The first is a description of the Jovian field at Europa that drives the induction. This model is identical to that used in the Gauss inversion technique – a spatially uniform field near Europa with a static background component and sinusoidally oscillating components at key frequencies. In retrievals performed on synthetic data, we find that at least seven of the highest amplitude frequencies are typically required to reduce inaccuracy to ~ 1 nT.

The second model component is Europa's internal structure. We adopt a spherically symmetric, three-layer model (e.g., Zimmer et al. 2000), with a liquid ocean of uniform conductivity sandwiched between the non-conducting mantle and the ice shell. Together, the internal structure and Jovian field models are used to calculate the induced dipole resulting from oscillation at each of the key frequencies (e.g., Parkinson 1983). Model solutions, therefore, must self-consistently match the phase and amplitude of the measured induced field at each frequency, thereby breaking the degeneracy that remains in the single-frequency case.

The third component of the retrieval model describes noise sources in the data (other than noise associated with plasma currents), primarily systematic sensor offsets and white noise. The sensor offsets are assumed to drift linearly during the mission and the white noise parameter, which describes the magnitude of all remaining scatter in the data, is assumed constant.

All three components are combined to produce a model of the observed magnetic field for the Europa Clipper tour, which is then compared to the observed data to generate the posterior probability distribution. We sample this distribution using Markov Chain Monte Carlo methods, which explore the model parameter space efficiently, evaluating how well a particular choice of model parameters matches the data (Foreman-Mackey et al. 2013; Salvatier et al. 2016).

In order to evaluate this analysis technique, we performed retrievals on synthetic datasets for a range of plausible European interiors (Biersteker et al. 2023). These data sets are similar to those used to test the iterative inversion method, but, in addition, specify a physical European interior model, sensor flicker and white noise, and drifting sensor offsets as input parameters. The synthetic datasets are generated for European interiors with ice shell thicknesses ranging from 2–30 km, ocean thicknesses of 50–168 km, and conductivities of $0.1\text{--}28\text{ S m}^{-1}$, spanning the range permitted by the Galileo measurements (Anderson et al. 1998; Billings and Kattenhorn 2005; Hand and Chyba 2007). In these retrievals, we adopt uniform input values for the log conductivity, ice thickness, and total water layer (ice and ocean) thickness. We deem retrievals to be successful if the input value is recovered within the 95% confidence interval of the posterior distribution. If the true value falls only inside the 99.7% interval, the retrieval is marginal. If the true value is not captured in these ranges the recovery of that parameter is deemed a failure. Using the Bayesian framework, we find

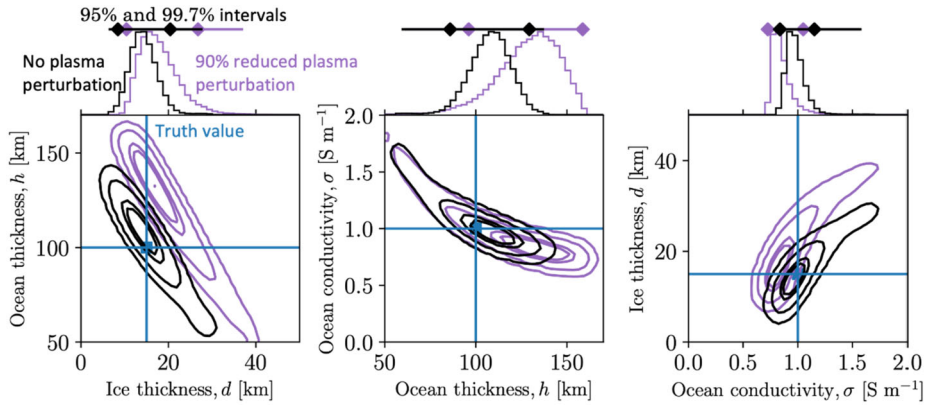


Fig. 19 Recovered ocean parameters from a simulated Europa Clipper tour with perfect (black) and partial (90%) (purple) corrections for moon-plasma interaction fields. Two-dimensional histograms show the posterior probabilities for each pairing of the three ocean parameters (ice thickness, ocean thickness, ocean conductivity). The corresponding one-dimensional histograms show the posterior probability distribution for the parameter on the x-axis. The 95% and 99.7% credible intervals are indicated by diamonds and the bar, respectively. The input values used to generate the dataset are indicated by vertical blue lines and the posterior probability and 95% interval are shown in black. All three ocean parameters are successfully recovered to within $\pm 50\%$

that the ECM will be able to recover Europa’s internal structure from typical model tours (40 to 50 flybys) for all of the tested scenarios at the 95% confidence level (black contours in Fig. 19). We have not tested the model using fewer flybys but anticipate successful retrieval from partial tours, just as for the Gauss inversion method.

A satisfactory inversion should be relatively insensitive to magnetic signals arising from the moon-plasma interaction, characterized to a good approximation by the MHD model described in Sect. 8.2. Such signals can mask or mimic some aspects of the induction response. Modeled contributions of plasma-generated fields will be removed from the measured fields prior to inversion but, as noted, the models are approximations. In order to establish the effects of residual plasma noise on the recovery of the induced field, a modified data set that included 10% of the modeled magnetic perturbations arising from plasma currents was also analyzed (purple contours in Fig. 19). Estimates of ocean thickness and conductivity changed little, but the recovered ice shell thickness changed significantly. The errors introduced by the plasma perturbation are found to depend significantly on the internal structure of Europa assumed in generating the synthetic dataset. We find that performance is most robust for modest (~ 1 S/m) conductivities, which are likely to be representative of Europa’s ocean. Our test data sets assumed imperfect sensor calibration and included spacecraft field contributions, but if the noise environment is worse than predicted (Sect. 6), the recovery of the physical parameters of interest by the Bayesian inversion approach will be less successful. However, it is likely that the data from the ice-penetrating radar will provide constraints on the ice shell thickness and thereby reduce the residual uncertainty of the inversion.

8.2 Plasma interaction modeling support

Deep inside Jupiter’s magnetosphere at the orbit of Europa, the corotating Jovian plasma continually flows towards the moon from its trailing hemisphere. The interaction of Jupiter’s magnetospheric plasma with Europa and its extended atmosphere produces electric currents

and associated magnetic perturbations that modify the total magnetic field measured in its vicinity. The signals of interest can be better identified if the magnetic perturbations associated with the plasma interaction can be characterized and removed from the total measured field prior to extracting the induction signal. For this purpose, a multi-fluid MHD model has been developed to simulate the magnetic fields arising from plasma interactions in Europa's space environment (Harris et al. 2021). Because the magnetic field arising from the plasma interaction varies in strength and spatial scale depending on the local conditions of the magnetosphere, multiple simulations using different input parameters are required to represent conditions that will be encountered at Europa on different orbits.

Near Europa, the gyroradii of the ions of Jupiter's magnetospheric plasma (~ 14 km for 100-eV O^+ in a 400 nT background field) are small relative to Europa's radius. Consequently, MHD codes are well-suited to model the plasma interaction by approximating the various plasma populations as conducting fluids. Harris et al. (2021) developed a multi-fluid MHD model that solves the mass, momentum, and pressure MHD equations for three fluids dominated by different ions: the thermal Jovian magnetospheric O^+ ions, and the O_2^+ and O^+ ions generated from Europa's atmosphere. The model also solves a separate electron pressure equation, enabling an inference of the electron temperature throughout the plasma. The model relies on the BATS-R-US MHD framework (Toth et al. 2012) and builds on the model by Rubin et al. (2015). The model calculates various source and loss terms added to the MHD equations to represent the effects of electron impact ionization, photoionization, charge exchange, and recombination based on the bulk properties of the ion and electron fluids, as well as the neutral density from a prescribed neutral atmosphere. The parameters of the model atmosphere (surface density, scale height, and longitudinal asymmetry) are constrained by measurements of the O_2 column density (Hall et al. 1995, 1998) and informed by prior models for the atmosphere (e.g., Cassidy et al. 2013). For each simulation, the induced magnetic field of Europa's ocean is represented by a dipole centered at Europa, with the direction and strength of the dipole calculated assuming completely efficient induction in a spherical subsurface ocean with a given radius, which is typically approximated to be the moon's radius according to Galileo observations (e.g., Zimmer et al. 2000). For these assumptions, at the pole of the induced dipole, the field is equal and opposite to the driving field.

The model solves for a steady-state solution representing Europa's plasma interaction for a given set of upstream plasma and field conditions. Figure 20 shows the density of the three ion fluids and the magnetic field components in the $Z = 0$ plane for a simulation of the Galileo E4 flyby. The local magnetic field and plasma parameters of Jupiter's magnetosphere are expected to change on timescales of several hours, much longer than the ~ 1 hour that Europa Clipper will spend in Europa's vicinity during each encounter. Therefore, steady-state solutions will adequately describe the plasma-related magnetic perturbations that must be removed from the total magnetic field in order to improve the retrieval of the induction signal. Figure 21 shows that, if even some portion of plasma noise remains after correcting the data by use of the MHD model, a correction for plasma allows the induced dipole signature to dominate the perturbations near Europa.

For each flyby, measurements provided by ECM and other instruments will provide the model boundary conditions that characterize the Jovian plasma and the neutral atmosphere at the outer and inner boundaries of the simulation domain (see Sect. 8.3). At the outer boundary, the magnetic field and plasma density, velocity, and temperature will be specified based on the observations from ECM and PIMS. At the inner boundary, the parameters of the prescribed induced dipole will be calculated based on the magnetospheric magnetic field imposed on Europa, and the parameters of the model atmosphere will be established

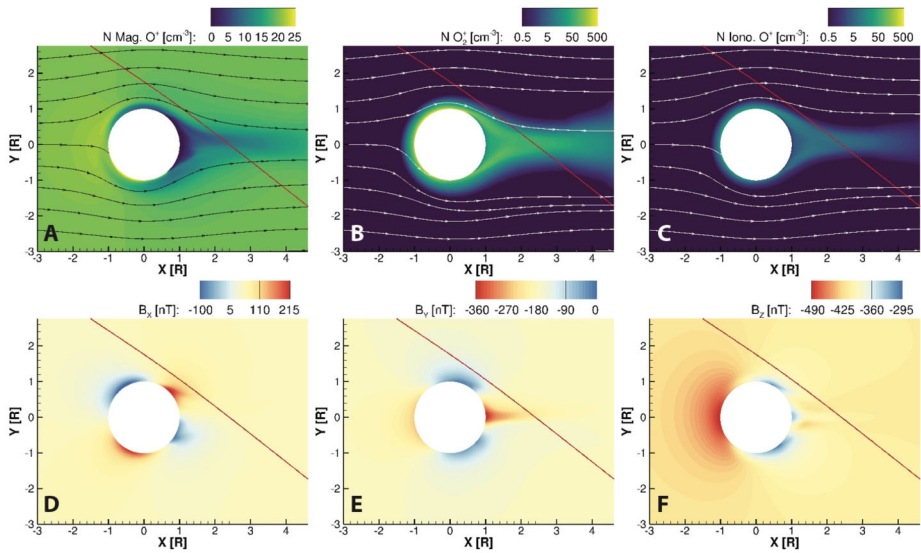


Fig. 20 Density contours of the three ion fluids and the magnetic field components in the $Z = 0$ plane from the Harris et al. (2021) simulation of the Galileo E4 flyby. The top row shows the density of the (A) magnetospheric O^+ , (B) ionospheric O_2^+ , and (C) ionospheric O^+ fluids and the lines with arrows show plasma flow streamlines of the corresponding ion fluids. The bottom row of panels shows the (D) B_x , (E) B_y , and (F) B_z components of the magnetic field. In all panels the trajectory of the E4 flyby is marked by a red line

using observations from the Europa Ultraviolet Spectrograph (Europa-UVS) and the Mass Spectrometer for Planetary Exploration (MASPEX) investigations (Waite et al. 2024 this collection).

The simulations of the magnetic perturbations arising from the plasma interaction will be subtracted from the total magnetic field measured by the ECM prior to the analysis of the dipolar signal of the ocean-induced magnetic field. Comparison of the 3D simulation results with data from PIMS will characterize the short-scale variability of plasma and magnetic field perturbations of the plasma interaction during each encounter. If Europa Clipper observes anomalous magnetic field or plasma signatures, such as the plume-generated magnetic perturbations detected by Galileo during its E12 flyby (Jia et al. 2018), 3D MHD modeling will provide a powerful tool for interpreting the observations.

In situ observations by ECM and PIMS will be compared with the simulated magnetic field and bulk plasma properties during each encounter and the model as well as the modeled dipole response will be iteratively modified to improve agreement with measurements.

8.3 Complementary data from PIMS and its use for induction modeling

Figure 21 demonstrates that the moon-plasma interaction obscures the measured signal of Europa's induced field and why this must be corrected in order to extract the magnetic signature of Europa's ocean. As described in the previous section, the MHD model will rely on data returned from other Europa Clipper instrumentation to inform inputs into the model so that the plasma perturbation can be appropriately simulated. Here, we describe more explicitly the complementary science that will aid the magnetometer investigation.

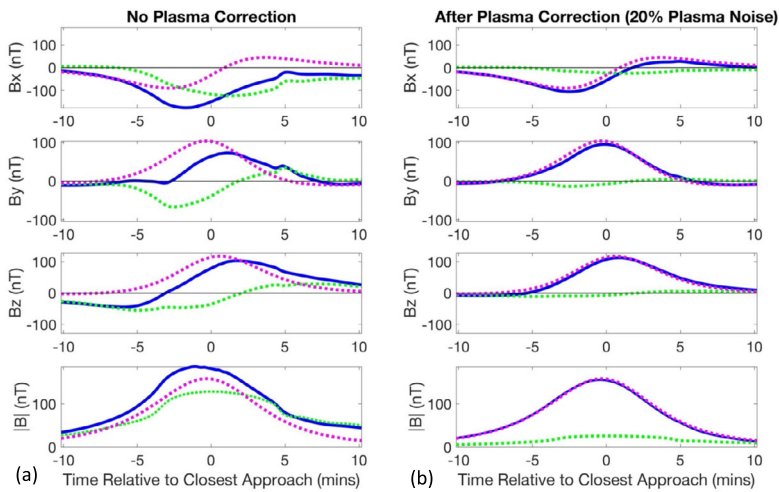


Fig. 21 The components and magnitude of the magnetic field perturbations extracted from a simulation of the interaction region (Fig. 19) along a nominal Europa Clipper flyby near closest approach. **(a)** The dashed magenta line shows the perturbation from Europa's induced magnetic field, the green dashed line shows the perturbations arising from currents flowing in the plasma, and the blue line shows the total perturbation. **(b)** The perturbations arising from plasma currents (green) have been reduced to 20% of the modeled values, thus mimicking the unmodeled contributions of such currents, the induced field (magenta) is unchanged, and the remaining perturbation (blue) is now dominated by the induced field

8.3.1 Magnetospheric plasma and ionosphere

PIMS data will be central to understanding how the properties of the magnetospheric plasma that interacts with Europa vary with time and location in Jupiter's plasma torus. PIMS will measure the density, velocity, and temperature of the thermal plasma (<10 keV ions and <2 keV electrons) on each flyby (Westlake et al. 2023 this collection). The magnetospheric plasma is significantly perturbed in Europa's vicinity and changes in its density and flow velocity affect the magnetic field (Harris et al. 2021). Near closest approach, PIMS will also directly sample the ionosphere and measure the density and temperature of ionospheric ions and electrons below 50 eV. Simultaneous observations of the ionosphere will be provided by REASON, which will determine the total electron content (TEC) below the spacecraft by measuring delays in the radar signal that are caused by ionospheric electrons. These two data products will characterize the ionosphere, whose properties are also significant as input for the simulations.

8.3.2 Neutral atmosphere

Europa's neutral atmosphere serves as the source of ionospheric ions, some of which are picked up by the magnetospheric plasma. Therefore, the global distribution of the neutral atmosphere affects the overall plasma interaction. Europa's neutral atmosphere is believed to be dominantly produced by sputtering from the water ice surface by energetic ions and electrons as well as the thermal plasma (Johnson et al. 2009; Cassidy et al. 2013). Sublimation modifies the distribution of the atmosphere (Johnson et al. 2009), and this contribution will vary in its position and amplitude as tidally locked Europa orbits Jupiter (Oza et al. 2019). Europa Clipper will determine the global structure of the atmosphere and how its

distribution varies in time with changing plasma and illumination conditions. Stellar occultations monitored by Europa-UVS will measure absorption features in the spectra of reference stars, and these measurements will identify the neutral species present in Europa's atmosphere and their corresponding densities. Complementary measurements will be provided by MASPEX, a mass spectrometer that will analyze atmospheric gases detected at the spacecraft's location. These data will be used in improved models of Europa's global atmospheric structure (Teolis et al. 2017; Harris et al. 2022).

8.3.3 Plumes

The application of an MHD model to data acquired on Galileo's Europa E12 flyby has shown that the magnetic signature seen during closest approach is consistent with the presence of a plume (Jia et al. 2018). Various instruments on Europa Clipper can detect and characterize such a plume (if present) and establish the properties that produce magnetic perturbations. Europa-UVS will be able to detect a plume by measuring enhanced Lyman alpha emissions caused by electron impact on the water particles of which it is composed. Additionally, the plume may be directly sampled by MASPEX, Surface Dust Analyzer (SUDA) (Kempf et al. [in prep](#)), and PIMS, all of which may detect enhancements in gases, dust, and ions.

8.4 Jupiter's magnetosphere and satellite interactions

8.4.1 Using magnetic field measurements to constrain Europa's interaction with Jupiter's magnetosphere

Data acquired very near Europa will provide insight into the moon's internal structure and possibly contribute to identifying localized eruptions of vapor, whereas data acquired elsewhere in approximately elliptical orbits around Jupiter (at lower time resolution) will be useful for understanding field and plasma dynamics of the middle magnetosphere of Jupiter. The data will be acquired in a region of the near equatorial magnetosphere previously explored by Galileo and other flyby missions. Many periapses will be close to Europa's orbit (in the prime mission, periapses range from 9.2 to 9.5 R_J and apoapses range from 38.3 to 52.7 R_J). The plot in Fig. 22 uses orbits from candidate tour 21F31V3. The data acquired in this or a similar tour will form the basis for studies of Europa's extended wake and the dynamics of the outer portion of the Io plasma torus.

Plasma measurements from Pioneer 10 revealed localized regions of enhanced plasma density somewhat outside of Europa's orbit and near the center of the plasma sheet (Intriligator and Miller 1982). The region of increased density was interpreted as an extended Europa plasma wake that slowly drifts radially outward as the moon moves through local time. The same region downstream of Europa and outside of its orbit was also identified through its magnetic signature in Galileo data by Russell et al. (1999) who inferred a radial displacement speed of 3 km/s. Russell et al. use the term "plume" to describe this feature. In order to distinguish this feature from the putative localized vapor eruptions from Europa's surface that are also referred to as plumes, we propose to use the term "Europa's plasma torus" for the extended region of enhanced plasma density and to reserve the term plume for near-surface phenomena. Europa Clipper will cross the Europa torus region both inbound (relatively close to the source at Europa) and outbound (where the density enhancement, if present, will imply that there is an almost complete torus around Jupiter). It will be of special interest to establish whether the rate of outward displacement varies from pass to pass

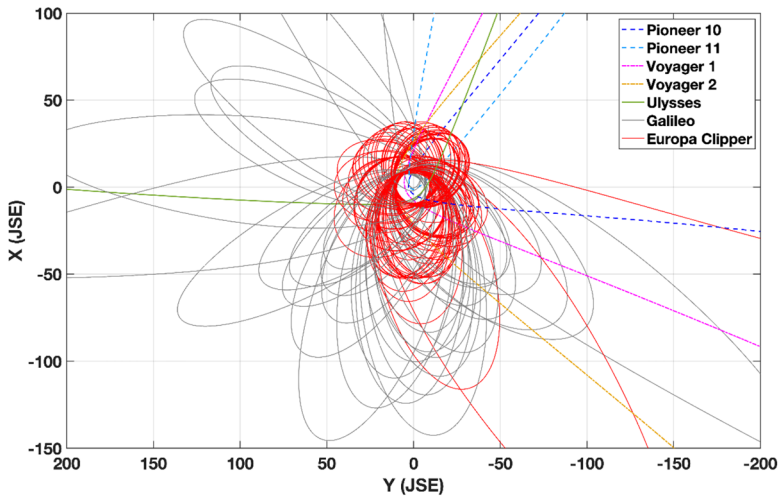


Fig. 22 The primary portion of a representative Europa Clipper tour (21F30V2) superimposed on a plot of Galileo's orbital coverage and other spacecraft orbits in the near equatorial Jovian magnetosphere

and to establish whether the variation relates to local time or to changing properties of Io's plasma torus or other aspects of magnetospheric dynamics.

Outward transport of plasma and magnetic flux is required in order to understand the relative stability of the Io plasma torus. The conservation of magnetic flux requires that the outward transport be balanced by inward transport, a process described as interchange. Near Io, flux tubes depleted of thermal plasma were identified as inward-moving flux tubes (Bolton et al. 1997; Kivelson et al. 1997; Thorne et al. 1997; Frank and Paterson 2000). ECM measurements of the magnetic field, in conjunction with PIMS measurements of the plasma density, will seek to establish the nature of interchange in a different part of the Io plasma torus, near and beyond the orbit of Europa.

The Europa Clipper mission is expected to arrive at Jupiter shortly before ESA's JUICE (JUper ICy moon Explorer) mission (Grasset et al. 2013). There will be intervals when JUICE is in the solar wind and Europa Clipper is in Jupiter's magnetosphere. This will provide an extended opportunity to acquire simultaneous data from a solar wind monitor and a spacecraft in Jupiter's magnetosphere, a situation that will greatly advance our understanding of the degree to which solar wind conditions control magnetospheric dynamics in a system that is largely driven by internal processes. There is a high probability that two-point measurements made by Europa Clipper and JUICE during the lengthy interval prior to its capture by Ganymede when both spacecraft are in the Jovian magnetosphere will provide data useful for establishing features of plasma transport and both missions plan to encourage such collaborative studies.

The currently planned tour includes seven passes by Ganymede and nine passes by Callisto. These flybys will give valuable data on the internal field of Ganymede and the inductive responses of both moons and will supplement new data to be acquired by ESA's JUICE mission.

8.4.2 Measurement of ion cyclotron waves for deriving composition of Europa's atmosphere and plumes

The interaction of Europa with the flowing plasma and energetic particles in Jupiter's magnetosphere leads to ionization of atmospheric neutral particles and sputtering of ions from Europa's surface, as discussed above. The newly ionized particles are picked up by the flowing plasma and, where plentiful, create unstable (non-isotropic-non-Maxwellian) particle distributions. Unstable distributions may then generate ion cyclotron waves, usually circularly polarized electromagnetic waves at frequencies typically below the ion gyrofrequency $f_g = qB/2\pi m$, where q is the charge on the ion, B is the field magnitude, and m is the ion mass. Positively charged ions typically generate left-hand circularly polarized waves, whereas negatively charged ions generate right-hand circularly polarized waves. The distinct frequency (from a fraction of a Hz to a few Hz near Europa) associated with a given mass per unit charge provides significant constraints on atmospheric and surface composition. For example, near Europa, Volwerk et al. (2001) identified ion cyclotron waves in the Galileo data that were associated with the positively-charged oxygen, sodium, SO₂ and potassium ions and negatively-charged chlorine. The ECM will observe the distribution of ion cyclotron waves in the vicinity of Europa and thus contribute to our understanding of the composition of Europa's atmosphere and surface layers and the distribution of the atmosphere.

9 Final words

This paper provides an overview of the planning, design, development, testing, and analysis that has gone into the Europa Clipper Magnetometer investigation. These efforts have been guided by the goals set for scientific exploitation of the data that will be collected during the years of the mission. Many team members have contributed to the effort with a level of expertise that would be hard to surpass. That the team has been able to design, build, and deliver an instrument, plan for testing and use, and develop sophisticated plans for extracting critical information about processes in a remote magnetosphere while simultaneously dealing with the challenge of living through an international pandemic is even more impressive.

Forecasts are rarely correct, so we should refrain from providing any, but it is tempting to challenge fate by stating the obvious. We know what we hope to learn from measurements to be made in the decade of the 2030s after the Europa Clipper reaches the Jovian system. Those are the known unknowns such as ice thickness and ocean depth at Europa that are discussed in detail in this paper. However, there are also the unknown unknowns (Rumsfeld 2011). Those are worth dreaming about and waiting for with impatience as the development, deployment, travel, and arrival at Europa bring ECM to its intended destination. We have no doubt that unanticipated discoveries await the arrival of the spacecraft and its complement of instruments.

Acknowledgements The authors thank the many engineers and scientists who contributed to the development of the ECM investigation and continue to do so. In particular, we thank Brian Cooke (JPL) who supported our efforts to obtain a longer boom and thereby set us on a path to success in our undertakings. We are extremely grateful to John Pearson (JPL), who provided strong leadership in resolving unanticipated problems first detected during environmental testing and a commitment to assuring the ECM will satisfy the demanding requirements of the Europa Clipper mission. We also thank Jodie Barker Ream (MIT) for her contributions to the Monte Carlo analysis and David Leneman (UCLA), and Jonathan Sauder and Hsin-Yi Hao (JPL) for sensor mechanical design and analyses and materials engineering. We thank Ed Gonzales (JPL) and his team for contributions to the analysis of sources of electromagnetic interference and Katherine Dang (JPL) for

her dedicated contributions to magnetics testing. The sensors were built at UCLA under exceptionally challenging conditions by Kyle Stewart, Henry Gonzalez, Michael Lawson, William Greer, Vicente Capistrano, Ryan Caron and Ryan Seaton, with support from Eric Orrill (Bison Aerospace), Christopher Ruiz (JPL), and Keyana Willcox (JPL). This work was supported by the National Aeronautics and Space Agency through the Europa Clipper Project under contract #1631492 through the Jet Propulsion Laboratory.

Declarations

Competing Interests The authors have no relevant financial or non-financial interests to disclose.

Open Access This article is licensed under a Creative Commons Attribution 4.0 International License, which permits use, sharing, adaptation, distribution and reproduction in any medium or format, as long as you give appropriate credit to the original author(s) and the source, provide a link to the Creative Commons licence, and indicate if changes were made. The images or other third party material in this article are included in the article's Creative Commons licence, unless indicated otherwise in a credit line to the material. If material is not included in the article's Creative Commons licence and your intended use is not permitted by statutory regulation or exceeds the permitted use, you will need to obtain permission directly from the copyright holder. To view a copy of this licence, visit <http://creativecommons.org/licenses/by/4.0/>.

References

- Acton CH Jr (1996) Ancillary data services of NASA's Navigation and Ancillary Information Facility. *Planet Space* 44:65. [https://doi.org/10.1016/0032-0633\(95\)00107-7](https://doi.org/10.1016/0032-0633(95)00107-7)
- Acuña MH (2004) The design, construction and test of magnetically clean spacecraft-A practical guide. NASA/GSFC internal report
- Andersen A, Kim W, McClure S, Jun I (2020) Monte Carlo evaluation of the Europa Clipper TID margin based on the variability of the Jovian radiation environment with application for mission design. *Space Weather* 1:e2019SW002340. <https://doi.org/10.1029/2019SW002340>
- Anderson JD, Schubert G, Jacobson RA, Lau EL, Moore WB, Sjogren WL (1998) Europa's differentiated internal structure: Inference from Galileo encounters. *Science* 281:219–222
- Banfield D, Rodriguez-Manfredi JA, Russell CT, Rowe KM, Leneman D, Lai HR, Cruce PR et al (2019) InSight auxiliary payload sensor suite (APSS). *Space Sci Rev* 215:4. <https://doi.org/10.1007/s11214-018-0570-x>
- Belcher JW (1973) A variation of the Davis-Smith method for in-flight determination of spacecraft magnetic fields. *J Geophys Res* 78:6480. <https://doi.org/10.1029/JA078i028p06480>
- Biersteker JB, Weiss BP, Cochrane C, Harris CDK, Jia X, Khurana KK, Liu J et al (2021) Revealing the internal structure of Europa with a Bayesian approach to magnetic induction studies. In: LPSC52, 2654
- Biersteker JB, Weiss BP, Cochrane C, Harris CDK, Jia X, Khurana KK, Liu J et al (2023) Revealing the interior structure of icy moons with a Bayesian approach to magnetic induction measurements. *Planet Sci J* 4:62. <https://doi.org/10.3847/PSJ/acc331>
- Billings SE, Kattenhorn SA (2005) The great thickness debate: Ice shell thickness models for Europa and comparisons with estimates based on flexure at ridges. *Icarus* 177:397–412. <https://doi.org/10.1016/j.icarus.2005.03.013>
- Blankenship DD, Mousessian A, Chapin E, Young DA, Patterson GW, Plaut JJ, Freedman AP et al Radar for Europa Assessment and Sounding: Ocean to Near-surface (REASON). this collection
- Bolton SJ, Thorne RM, Gurnett DA, Kurth WS, Williams DJ (1997) Enhanced whistler-mode emissions: Signatures of interchange motion in the Io torus. *Geophys Res Lett* 24:2123
- Bowden M, Benton M (1993) Design of deployable-truss masts for space station. In: Aerospace Design Conference, Irvine, CA, 16–19 February, 1993. <https://doi.org/10.2514/6.1993-975>. published online 17 Aug 2012
- Cao H, Dougherty MK, Hunt G, Provan G, Cowley SWH, Kellock S, Stevenson DJ (2020) The landscape of Saturn's internal magnetic field from the Cassini Grand Finale. *Icarus* 344:113541. <https://doi.org/10.1016/j.icarus.2019.113541>
- Casajus LG, Zannoni M, Modenini D, Tortora P, Nimmo F, van Hoolst T, Buccino D et al (2021) Updated Europa gravity field and interior structure from a reanalysis of Galileo tracking data. *Icarus* 358:114187. <https://doi.org/10.1016/j.icarus.2020.114187>
- Cassidy TA, Paranicas CP, Shirley JH, Dalton JB, Teolis BD, Johnson RE, Kamp L et al (2013) Magnetospheric ion sputtering and water ice grain size at Europa. *Planet Space Sci*. <https://doi.org/10.1016/j.pss.2012.07.008>


- Cochrane CJ, Murphy N, Raymond CA, Biersteker JB, Dang K, Jia X, Korth H, Narvaez P, Ream JB, Weiss BP (2023) Magnetic field modeling and visualization of the Europa Clipper spacecraft. *Space Sci Rev*. accepted for publication
- Colburn DS, Reynolds RT (1985) Electrolytic currents in Europa. *Icarus* 63:39–44
- Coleman TF, Li Y (1994) On the convergence of reflective Newton methods for large-scale nonlinear minimization subject to bounds. *Mathematical Programming* 67:189–224
- Coleman TF, Li Y (1996) An interior, trust region approach for nonlinear minimization subject to bounds. *SIAM Journal on Optimization* 6:418–445
- Davis L Jr, Smith EJ (1968) The in-flight determination of spacecraft field zeros. *Eos Trans AGU* 49:257
- Dessler AJ (1983) Coordinate systems, Appendix B. In: Dessler AJ (ed) *The physics of the Jovian magnetosphere*. Cambridge University Press, New York, pp 498–504
- Foreman-Mackey D, Hogg DW, Lang D, Goodman J (2013) emcee: The MCMC Hammer. *PASP* 125:306
- Frank LA, Paterson WR (2000) Observations of plasmas in the Io torus with the Galileo spacecraft. *J Geophys Res* 105:16017–16034
- Grasset O, Dougherty MK, Coustenis A, Bunce EJ et al (2013) Jupiter Icy moons Explorer (JUICE): An ESA mission to orbit Ganymede and to characterize the Jupiter system. *Planet Space Sci* 78:1–21. <https://doi.org/10.1016/j.pss.2012.12.002>
- Grotenhuis M, Studer R, Carter D, Dence R, Wolf M, Mandi J (2019) Lessons learned from flight observations of the GOES-R magnetometer. In: 2019 ESA Workshop on Aerospace EMC (Aerospace EMC)
- Hall DT, Strobel DF, Feldman PD, McGrath MA, Weaver HA (1995) Detection of an oxygen atmosphere on Jupiter's moon Europa. *Nature* 373:677–679. <https://doi.org/10.1038/373677a0>
- Hall DT, Feldman PE, McGrath MA, Strobel DF (1998) The far-ultraviolet oxygen airglow of Europa and Ganymede. *Astrophys J* 499(1):475–481. <https://doi.org/10.1086/305604>
- Hand KP, Chyba F (2007) Empirical constraints on the salinity of the European ocean and implications for a thin ice shell. *Icarus* 189:424–438
- Harris CDK, Jia X, Slavin JA, Toth G, Huang Z, Rubin M (2021) Multi-fluid MHD simulations of Europa's plasma interaction under different magnetospheric conditions. *J Geophys Res* 126:e2020JA028888
- Harris CDK, Jia X, Slavin JA (2022) Multi-fluid MHD simulations of Europa's plasma interaction: Effects of variation in Europa's atmosphere. *J Geophys Res* 127:e2022JA030569. <https://doi.org/10.1029/2022JA030569>
- Hurwitz L (1960) Eccentric dipoles and spherical harmonic analysis. *J Geophys Res* 65:2555–2556
- Intriligator DS, Miller WD (1982) First evidence for a Europa plasma torus. *J Geophys Res* 87:8081–8090
- Jacobson RA, Haw RJ, McElrath TP, Antreasian PG (1999) A comprehensive orbit reconstruction for the Galileo Prime Mission in the J2000 system. In: AAS/AIAA Astrodynamics Specialist Conference. American Astronautical Society, Girdwood, Alaska
- Jager T, Leger JM, Fratter I, Lier P, Pacholczyk P (2016) Magnetic cleanliness and thermomagnetic effect: Case study of the absolute scalar magnetometer and its environment on swarm satellites. In: 2016 ESA Workshop on Aerospace EMC (Aerospace EMC), pp 1–6. <https://doi.org/10.1109/AeroEMC.2016.7504584>
- Jia X, Kivelson MG, Khurana KK, Kurth WS (2018) Evidence of a plume on Europa from Galileo magnetic and plasma waves signatures. *Nature Astron* 2:459–464
- Johnson RE, Burger MH, Cassidy TA, Leblanc F, Marconi M, Smyth WH (2009) Composition and detection of Europa's sputter-induced atmosphere. In: Pappalardo RT, McKinnon WB, Khurana KK (eds) *Europa*, vol 21. University of Arizona Press, Tucson, pp 507–528
- Kargel JS, Consolmagno GJ (1996) Magnetic fields and the detectability of brine oceans in Jupiter's icy satellites. *Lunar Planet Sci XXVII*:643
- Kempf S, Tucker S, Altobelli N, Briois C, Cable ML, Grün E, Gudpati MS et al SUDA: A Surface Dust Analyser for compositional mapping of the Galilean moon Europa. this collection
- Kepko EL, Khurana KK, Kivelson MG, Elphic RC, Russell CT (1996) Accurate determination of magnetic field gradients from four point vector measurements: 1. Use of natural constraints on vector data obtained from a single spinning spacecraft. *IEEE Trans Magnetics* 32:377–385
- Khurana KK (1997) Euler potential models of Jupiter's magnetospheric field. *J Geophys Res* 102(A6):11295–11306. <https://doi.org/10.1029/97JA00563>
- Khurana KK, Tsyganenko NA (2002) A global model of Jupiter's magnetospheric field. Talk presented at the Fall AGU meeting, San Francisco
- Khurana KK, Kivelson MG, Stevenson DJ, Schubert G, Russell CT, Walker RJ, Joy S, Polansky C (1998) Induced magnetic fields as evidence for subsurface oceans in Europa and Callisto. *Nature* 395:777
- Khurana KK, Kivelson MG, Russell CT (2002) Searching for liquid water on Europa by using surface observatories. *Astrobiology* 2(1):93–103
- Khurana KK, Kivelson MG, Hand KP, Russell CT (2009) Electromagnetic induction from Europa's ocean and the deep interior. In: Pappalardo RT, McKinnon WB, Khurana KK (eds) *Europa*. University of Arizona Press, Tucson, pp 571–586. Chap. 24

- Kivelson MG, Khurana KK, Means JD, Russell CT, Snare RC (1992) The Galileo magnetic field investigation. *Space Sci Rev* 60: 357–383. <https://doi.org/10.1007/BF00216862>
- Kivelson MG, Khurana KK, Russell CT, Walker RJ (1997) Intermittent short-duration magnetic field anomalies in the Io torus: Evidence for plasma interchange? *Geophys Res Lett* 24:2127
- Kivelson MG, Khurana KK, Russell CT, Volwerk M, Walker RJ, Zimmer C (2000) Galileo magnetometer measurements strengthen the case for a subsurface ocean at Europa. *Science* 289:1340
- Korth H, Paczkowski B (2022) Europa Clipper Science Data Management Plan
- Leinweber HK, Russell CT, Torkar K, Zhang TL, Angelopoulos V (2008) An advanced approach to finding magnetometer zero levels in the interplanetary magnetic field. *Meas Sci Technol* 19:055104. <https://doi.org/10.1088/0957-0233/1019/055104>
- Levenberg K (1944) A method for the solution of certain problems in least-squares. *Quart Appl Math* 2:164–168
- Maghsoudi E, Sauder J, Nelson E, Pierce D, Mok M (2021) Europa Clipper Magnetometer thermal design evolution, validation, and verification. In: Proceedings of 50th International Conference on Environmental Systems (ICES), ICES-2021-356. <https://hdl.handle.net/2346/87271>
- Marquardt D (1963) An algorithm for least-squares estimation of nonlinear parameters. *SIAM Journal Applied Mathematics* 11:431–441
- Mazarico E, Buccino D, Castillo-Rogez J, Dombard AJ, Genova A, Hussmann H, Kiefer WS et al (2023) The Europa Clipper Gravity and Radio Science Investigation. *Space Sci Rev* 219:30. <https://doi.org/10.1007/s11214-023-00972-0>
- Mehlem K (1978a) Magnetostatic cleanliness analysis by the multiple dipole modelling method. In: Proc. First Spacecraft Electromagnetic Compatibility Seminar, pp 165–179
- Mehlem K (1978b) Multiple magnetic dipole modeling and prediction of satellites. *IEEE Trans Magn MAG-14*:1064–1071
- Mehlem K, Wiegand A (2010) Magnetostatic cleanliness of spacecraft. In: Proc. 2010 Asia-Pacific International Symposium on Electromagnetic Compatibility, pp 936–944
- Moré JJ (1977) The Levenberg-Marquardt algorithm: Implementation and theory. In: Watson GA (ed) Numerical Analysis. Lecture Notes in Mathematics, vol 630. Springer, Berlin, pp 105–116
- Neubauer FM, Schatten KH (1974) Theoretical and observational analysis of spacecraft fields. *J Geophys Res* 79:1550–1554
- Oza AV, Leblanc F, Johnson RE, Schmidt C, Leclercq L, Cassidy TA, Chaufray J-Y (2019) Dusk over dawn O₂ asymmetry in Europa’s near-surface atmosphere. *Planet Space Sci* 167:23–32
- Pan Y, Yong W, Secco RA (2021) Electrical conductivity of aqueous NaCl at high pressure and low temperature: Application to deep subsurface oceans of icy moons. *Geophys Res Lett* 48:e2021GL094020. <https://doi.org/10.1029/2021GL094020>
- Parkinson WD (1983) Introduction to geomagnetism. Scottish Academic Press, Edinburgh
- PDS (2021) Planetary data system standards reference version 1.16.0, JPL D-7669, Part 2. <https://pds.nasa.gov/datastandards/about/>
- Pellegrino S (2001) Deployable structures in engineering. In: Pellegrino S (ed) Deployable structures. International Centre for Mechanical Sciences, vol 412. Springer, Vienna, pp 1–35. https://doi.org/10.1007/978-3-7091-2584-7_1
- Roberts JH, McKinnon WB et al (2023) Exploring the interior of Europa with Europa Clipper. *Space Sci Rev* 219
- Roth L, Saur J, Retherford KD, Strobel DF, Feldman PD, McGrath MA, Nimmo F (2014) Transient water vapor at Europa’s south pole. *Science* 343:171–174. <https://doi.org/10.1126/science.1247051>
- Rubin M, Jia X, Altwegg K, Combi M, Daldorff LKS, Gombosi T, Khurana KK et al (2015) Self-consistent multifluid MHD simulations of Europa’s exospheric interaction with Jupiter’s magnetosphere. *J Geophys Res* 120:3503–3524. <https://doi.org/10.1002/2015JA021149>
- Rumsfeld D (2011) Known and Unknown: A Memoir, Penguin Group, New York. (cited in Wikipedia article: “There are known knowns”, January, 2022)
- Russell CT (1971) Geophysical coordinate transformations. *Cosmic Electrodynamic* 2:184
- Russell CT, Huddleston DE, Khurana KK, Kivelson MG (1999) The fluctuating magnetic field in the middle jovian magnetosphere: Initial Galileo observations. *Planet Space Sci* 47:133–142
- Russell CT, Anderson BJ, Baumjohann W, Bromund KR, Dearborn D, Fischer D et al (2016) The Magnetospheric Multiscale Magnetometers. *Space Sci Rev* 199:189–256. <https://doi.org/10.1007/s11214-014-0057-3>
- Salvatier J, Wiecki TV, Fonnesbeck C (2016) Probabilistic programming in Python using PyMC3. *PeerJ Comput Sci* 2:e55
- Schnurr R, Bonalsky T, Todirita M, Kornenwetter J, Early D, Grotenhuis M, Studer R et al (2019) Lessons learned from flight observations of the GOES-R Magnetometer. In: 2019 ESA Workshop on Aerospace EMC (Aerospace EMC), pp 1–6. <https://doi.org/10.23919/AeroEMC.2019.8788929>

- Schubert G, Jacobson RA, Lau EL, Moore WB, Sjogren WL (1998) Europa's differentiated internal structure: Inferences from four Galileo encounters. *Science* 281:2019
- Schubert G, Anderson JD, Spohn T, McKinnon WB (2004) Interior composition, structure and dynamics of the Galilean satellites. In: Bagenal F, Dowling TE, McKinnon WB (eds) *Jupiter: The Planet, Satellites, and Magnetosphere*, Cambridge University Press, pp 281–306
- Seufert M, Saur J, Neubauer FM (2011) Multi-frequency electromagnetic sounding of the Galilean moons. *Icarus* 214:477–494
- Smith EJ, Connor BV, Foster GT (1975) Measuring the magnetic fields of Jupiter and the outer solar system. *IEEE Transactions on Magnetics* MAG-11(4)
- Sparks WB, Hand KP, McGrath MA, Bergeron E, Cracraft M, Deustra SE (2016) Probing for evidence of plumes on Europa with HST/STIS. *Astrophys J* 829:121
- Teolis BD, Wyrick DY, Bouquet A, Magee BA, Waite JH (2017) Plume and surface feature structure and compositional effects on Europa's global exosphere: Preliminary Europa mission predictions. *Icarus* 284:18–29
- Thorne RM, Armstrong TP, Stone S, Williams DJ, McEntire RW, Bolton SJ, Gurnett DA et al (1997) Galileo evidence for rapid interchange transport in the Io torus. *Geophys Res Lett* 24:2131
- Toth G, van der Holst B, Sokolov IV, DeZeeuw DL, Gombosi TI, Fang F, Manchester WB et al (2012) Adaptive numerical algorithms in space weather modeling. *J Computational Phys* 231(3):870–903. <https://doi.org/10.1016/j.jcp.2011.02.006>
- Vance SD, Styczinski MJ, Bills BG, Cochrane CJ, Soderlund KM, Gomez-Perez N, Paty C (2021) Magnetic induction responses of Jupiter's ocean moons including effects from adiabatic convection. *J Geophys Res: Planets* 126:e2020JE006418. <https://doi.org/10.1029/2020JE006418>
- Volwerk M, Kivelson MG, Khurana KK (2001) Wave activity in Europa's wake: implications for ion pick-up. *J Geophys Res* 106:26033
- Waite JH, Burch JL, Brockwell TG, Young DT, Miller GP, Persyn SC, Stone JM et al (2024) MASPEX-Europa: The Europa Clipper neutral gas mass spectrometer investigation. *Space Sci Rev* 220
- Westlake JH, McNutt RL, Jun I et al (2023) Plasma Instrument for Magnetic Sounding (PIMS) on the Europa Clipper Mission. *Space Sci Rev* 219
- Zhang TL, Berghofer G, Magnes W, Delva M, Baumjohann W, Biernat H, Lichtenegger H et al (2007) MAG: The fluxgate magnetometer of Venus Express. *ESA Spec Pub* 1295:1–10
- Zimmer C, Khurana KK, Kivelson MG (2000) Subsurface oceans on Europa and Callisto: Constraints from Galileo magnetometer observations. *Icarus* 147:329
- Zolotov MY, Kargel J (2009) On the chemical composition of Europa's icy shell, ocean, and underlying rocks. In: Pappalardo RT, McKinnon WB, Khurana KK (eds) *Europa*. University of Arizona Press, Tucson, pp 431–458

Publisher's Note Springer Nature remains neutral with regard to jurisdictional claims in published maps and institutional affiliations.

Authors and Affiliations

Margaret G. Kivelson^{1,2}  · Xianzhe Jia² · Karen A. Lee³ · Carol A. Raymond³ · Krishan K. Khurana¹ · Mitchell O. Perley³ · John B. Biersteker⁴ · Jordana Blacksborg³ · Ryan Caron¹ · Corey J. Cochrane³ · Olivia R. Dawson³ · Camilla D.K. Harris^{2,3,5} · Jonathan E. Jones³ · Steven Joy¹ · Haje Korth⁶ · Jiang Liu¹ · Elham Maghsoudi³ · Neil Murphy³ · David Parsley³ · David R. Pierce³ · Caroline Racho³ · Ingo Richter⁷ · Christopher T. Russell¹ · Sarah Sherman³ · Robert J. Strangeway¹ · Mickey Villarreal^{3,8} · Benjamin P. Weiss⁴ · Lee Wigglesworth³

✉ M.G. Kivelson
mkivelson@igpp.ucla.edu

¹ Department of Earth, Planetary, and Space Sciences, University of California, Los Angeles, CA, USA

² Department of Climate and Space Science and Engineering, University of Michigan, Ann Arbor, MI, USA

- ³ Jet Propulsion Laboratory, California Institute of Technology, Pasadena, CA, USA
- ⁴ Department of Earth, Atmospheric and Planetary Sciences, Massachusetts Institute of Technology, Cambridge, MA, USA
- ⁵ Present address: Research Computing, University College London, London, UK
- ⁶ The Johns Hopkins University Applied Physics Laboratory, Laurel, MD, USA
- ⁷ Institute for Geophysics and Extraterrestrial Physics, Technical University of Braunschweig, Braunschweig, Germany
- ⁸ Present address: Northrop Grumman, Woodland Hills, CA, USA